Journal of Manufacturing Processes 127 (2024) 645–659

Contents lists available at ScienceDirect

Journal of Manufacturing Processes

journal homepage: www.elsevier.com/locate/manpro

Material removal mechanisms in ultra-high-speed scratching of Ti6Al4V alloy by selective laser melting

Qinghong Jiang [a,b,c], Shuai Li [a], Hao Liu [a], Mingwang Fu [b,*], Bi Zhang [a,*]

[a] Department of Mechanical and Energy Engineering, Southern University of Science and Technology, Shenzhen 518055, China
[b] Department of Mechanical Engineering, Research Institute of Advanced Manufacturing, The Hong Kong Polytechnic University, Hung Hom, Kowloon, Hong Kong, China
[c] Mindray Bio-medical Electronics Co. Ltd

ARTICLE INFO

Keywords:
Titanium alloy
Selective laser melting
Single-point scratching
Ultra-high-speed machining
Material removal mechanism

ABSTRACT

Selective laser melting (SLM) offers advanced solutions for manufacturing high added value titanium alloy (Ti-alloy) components, owing to its capability to facilitate rapid, integrated, and customisable manufacturing of complex parts. However, surface machining is imperative for SLM-manufactured (SLM-ed) components due to the poor surface integrity. SLM-ed Ti-alloy is a typical difficult-to-machine material, conventional machining methods are difficult to realize high-efficiency and high-quality machining of SLM-ed Ti-alloy. Ultra-high-speed machining (UHSM) exhibits immense potential for enhancing machining efficiency and quality. However, the material removal mechanism of SLM-ed Ti-alloy in ultra-high-speed regions remains unclear. This study develops a single-point scratching (SPS) system to investigate material removal mechanisms across speeds ranging from 20 m/s to 220 m/s. Systematic characterisations regarding surface creation, subsurface microstructure, and chip formation were conducted using FIB and STEM techniques. The results revealed that the pile-up effect was significantly suppressed at higher speeds. The machining-deformed zone (MDZ) exhibited a "skin effect," with plastic deformation confined to a superficial layer with a depth within 1 μm at 220 m/s. The deformation mechanism transitioned from dislocation-mediated deformation (DMD) to twin-mediated deformation (TMD) under extremely high strain rate conditions, leading to the formation of ultrafine grains with embedded twins (UGENTs) structure. Additionally, the chip removal mode progressively shift from continuous chips to segmented chips, and eventually to fragmented chips with increased scratching speed. This study provides an insight into the material removal and deformation process of SLM-ed Ti-alloy under low to ultra-high-speed deformations, and lays the theoretical basis for the high-efficiency and high-quality machining of difficult-to-machining materials.

1. Introduction

Ti-alloy is one of the most primary structural metallic materials due to its exceptional combination of high specific strength, extraordinary corrosion resistance, and excellent biocompatibility [1,2]. It has been increasingly applied in many critical industries, such as aerospace, navigation, automotive, and biomedicine [3]. However, the conventional manufacturing of Ti-alloy components usually involves protracted cycles and complex processes. This invariably results in notable material wastage, increased energy consumption, and pronounced environmental pollution. Moreover, conventional manufacturing is difficult to accommodate the rapid updates and improvements of modern products, posing challenges in the production of high-performance Ti-alloy components [4].

Recently, selective laser melting (SLM), one of the most prosperous metal additive manufacturing (AM) techniques, has attracted significant attention owing to its ability to manufacture high-value Ti-alloy components with high strength and integrated complex structures [5]. Meanwhile, SLM offers substantial advantages such as rapid prototyping, high material utilization, and the ability to create lightweight products [6]. Consequently, it is gradually evolving into an indispensable manufacturing technique for producing high-quality components [7]. Despite SLM manufactured (SLM-ed) components exhibiting better surface quality compared to their counterparts produced by other metal AM techniques, such as selective electron beam melting (SEBM) [8], wire and arc additive manufacturing (WAAM) [9], and laser engineering

* Corresponding authors.
E-mail addresses: ming.wang.fu@polyu.edu.hk (M. Fu), zhangb@sustech.edu.cn (B. Zhang).

https://doi.org/10.1016/j.jmapro.2024.07.145
Received 22 April 2024; Received in revised form 11 July 2024; Accepted 31 July 2024
Available online 14 August 2024

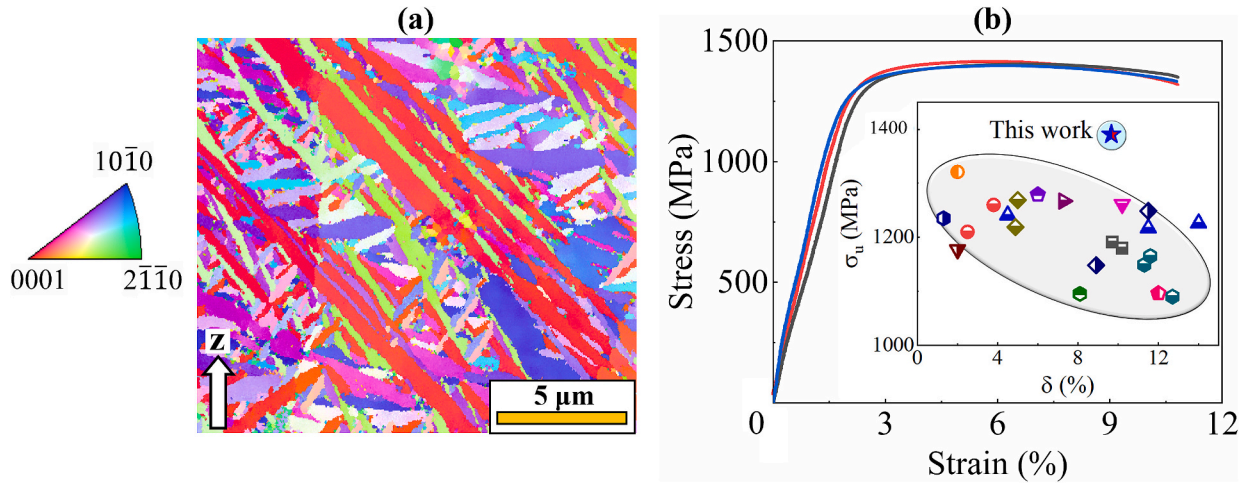

Fig. 1. (a) EBSD inverse pole figure (IPF) showing the lamellar α + β microstructure; (b) Stress-strain curves (The inset displays the tensile properties comparison with recent references) [29]. (Z direction is the building direction).

net shape (LENS) [10], the inherent poor surface quality of AM technology remains a persistent challenge limiting the widespread adoption of SLM. Generally, as-built SLM-ed components exhibit an average surface roughness (Ra) ranging from 5 to 40 μm [11], levels that are considered unacceptable for critical structural and functional components. Additionally, internal defects such as pores, cracks, and lack of fusion, are easily induced during the complex SLM process [12], particularly tending to distribute in the near-surface layer [13]. Therefore, surface machining becomes imperative to enhance surface finish and eliminate the defects in the surface layer [14].

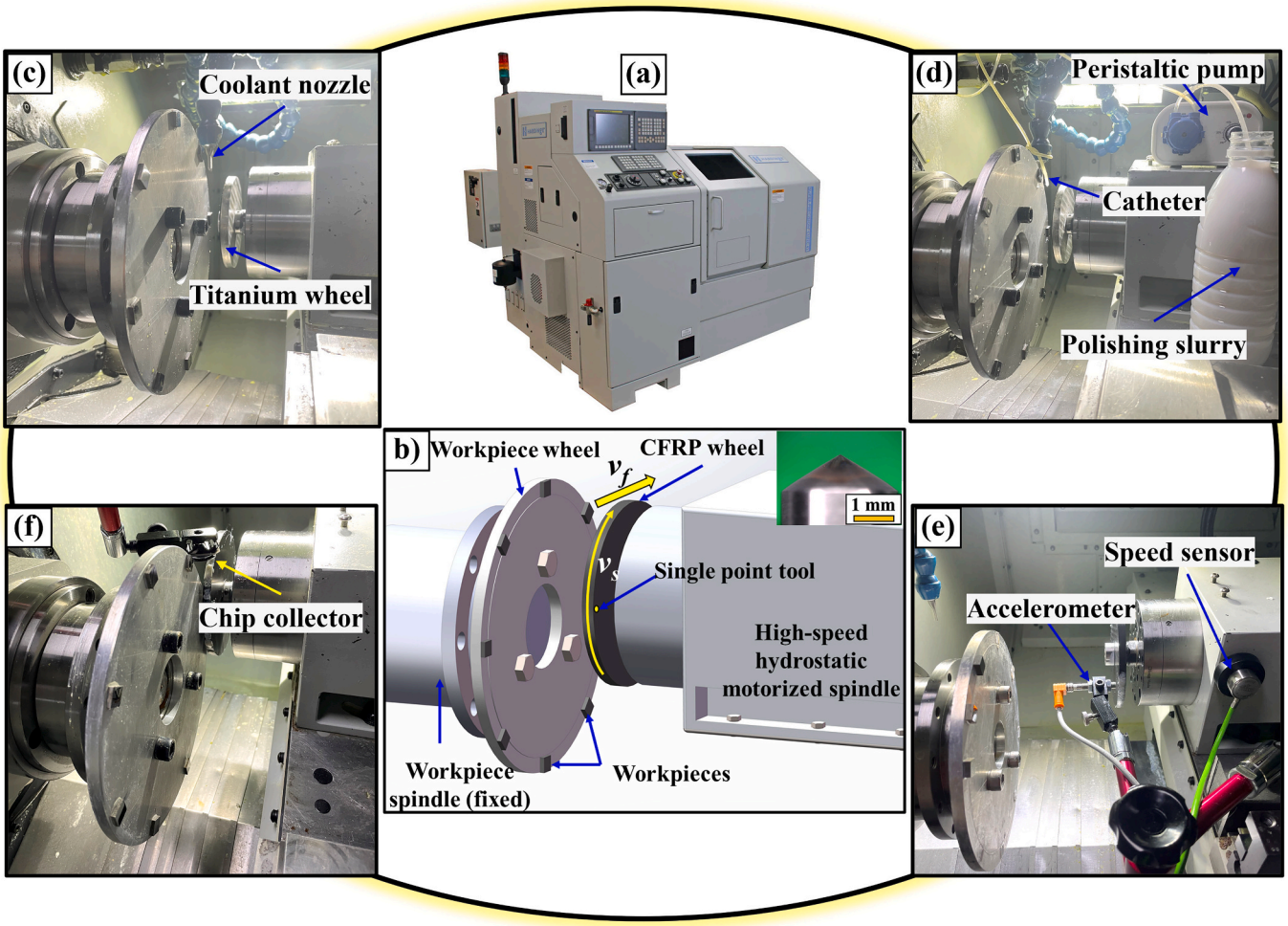

Fig. 2. Experimental setups: (a) Hardinge machine tool; (b) Schematic diagram of the single-point scratching. Preparation procedures: (c) On-process grinding; (d) On-process polishing; (e) On-process dynamic balance process. (f) Single-point scratching process.

However, Ti-alloy is recognized as a typical difficult-to-machine material due to its high strength, low thermal conductivity, and high chemical reactivity. The combined material characteristics result in accelerated tool wear, compromised surface integrity, and low material removal rate [15,16]. Furthermore, SLM-ed Ti-alloy possesses distinct refined microstructures and mechanical properties, such as higher strength, hardness, and residual stress compared to conventional Ti-alloy. These discrepancies result in different machining characteristics, introducing new machining challenges. Recent studies have demonstrated that conventional machining of SLM-ed Ti-alloy can induce higher cutting force, cutting temperature, and more severe tool wear [17–19]. Consequently, the conventional machining of SLM-ed Ti-alloy suffers from a dilemma between efficiency and quality, where achieving high-quality often requires sacrificing efficiency.

Ultra-high-speed machining (UHSM) is a promising technique to address the machining problems of SLM-ed Ti-alloy due to its ability to achieve both high-quality and high-efficiency simultaneously [20,21]. It has been demonstrated that the strain rate effect plays a key role in ultra-high-speed region. The plastic deformation can be significantly suppressed with an increase in strain rate, a ductile material might undergo a brittle fracture as the strain rate exceeded a critical value [22]. Zhang et.al [20] summarized the depth of subsurface damage (SSD) of different materials under different strain rate conditions, it concluded that the SSD was effectively reduced at a higher strain rate. Meanwhile, Guo et.al [23,24] demonstrated that the surface quality of both Al6061T6 alloy and Al/SiCp metal matrix composites can be improved in high-speed grinding.

However, different material dynamic responses can be involved in UHSM with strain rate reaching up to 10^7 s^{-1}. The mechanical properties and failure mechanisms are intimately connected to the strain rate of external loading [25,26]. Meanwhile, the microscale activities such as dislocation slip, twinning, and phase transformation can be altered under extreme loading conditions [27]. Consequently, the material removal mechanism, microstructure evolution, and damage mode undergo substantial changes, and the established understanding of these phenomena based on conventional machining may no longer be applicable in the UHSM region [28].

Although extensive research has been conducted to reveal the material removal and deformation mechanisms of Ti-alloy in the conventional speed region [29,30], exploring these topics in the UHSM region presents significant challenges. Conventional machining processes such as cutting, milling, and drilling are difficult to realize extremely high speeds [31,32]. While grinding process can achieve very high linear speed, it is difficult to investigate the material deformation and removal mechanisms during a grinding process due to the simultaneous and repetitive cutting of a large number of abrasive particles [33]. SPS is an effective technique for investigating material removal mechanism at the microscale. Nevertheless, the highest speed reported in previous research for SPS studies was 120 m/s due to limitations in experimental setup [34], which has not yet reached the UHSM region.

In tandem with these, a SPS system was designed and developed to achieve ultra-high-speed scratching. Based on which, a series of SPS tests from conventional to ultra-high-speed range (20–220 m/s) of SLM-ed Ti6Al4V experiments were conducted. Subsequently, this study applied focus ion beam system (FIB) + transmission electron microscope (TEM) techniques to investigate the material removal mechanism from the aspects of surface morphology/profile, subsurface deformation, and chip formation characteristics, aiming to elucidate mechanism transition of material deformation and microstructure evolution from conventional to extremely high speeds.

2. Experimental procedure and methodology

2.1. Working material and experimental setup

The SLM-ed Ti6Al4V samples with a high relative density (99.7 %) were manufactured using optimized SLM parameters (Laser power: 220 W; scanning speed: 1200 mm/s; hatch spacing: 80 μm; layer thickness: 30 μm) [35]. The microstructure was characterized by lamellar α + β with an average lath thickness of 282 nm (Fig. 1a). Furthermore, the SLM-ed Ti6Al4V exhibited superior tensile properties, with a high tensile strength of 1390 MPa, while maintaining a high elongation of 9.66 % simultaneously.

A SPS system was designed and developed based on a QuestGT27 grinding machine (Hardinge) equipped with a high-speed hydrostatic motorized spindle (Fig. 2a). The schematic diagram of the SPS system is shown in Fig. 2b. The SLM-ed Ti6Al4V samples (10×10×3 mm) were affixed onto a titanium wheel using paraffin wax. The conical single-point diamond tool, characterized by a tip radius of 30 μm and a cone angle of 120°, was mounted on a carbon fiber reinforced plastic (CFRP) wheel to achieve ultra-high-speed scratching. On-process grinding and polishing were applied to remove the coarse surface layer and ensure all scratch surfaces are on the same vertical plane (Abrasive papers from #180 to #3000 (Fig. 2c) and polishing cloth (Fig. 2d) were tailored and affixed on another titanium wheel to realize on-process grinding and polishing). Additionally, on-process dynamic balance was conducted to guarantee dynamic balancing performance (Fig. 2e). A sample stage with carbon tape was arranged above the sample to collect flying chips (Fig. 2f). The machining parameters are summarized in Table 1, the speed ratio of scratching linear speed and feed speed was fixed to produce evenly spaced parallel single scratches, and eight SPS trials with scratching linear speed velocity varying from 20 m/s to 220 m/s were carried out. Before each trial, a new single-point scratching tool was substituted.

Table 1
Machining parameters setting for SPS of Ti-alloy.

Trials	Scratching linear speed v_s (m/s)	Feed speed v_f (mm/min)	Depth of cut (μm)
1	20	313	2.5
2	60	938	
3	100	1563	
4	140	2188	
5	160	2500	
6	180	2813	
7	200	3125	
8	220	3438	

2.2. Material characterization methods

The machined scratches were analysed in terms of surface and subsurface. The surface morphology was detected by laser scanning confocal microscopy (LSCM), and the cross-sectional profiles were analysed by the MULTI-FILE ANALYSIS software. The focus ion beam (FIB: Helios 600i) and transmission electron microscope (Talos F200X G2) techniques were combined to reveal the subsurface microstructures. The large cross-sectional TEM lamellae were extracted to investigate the global distribution of the subsurface microstructure, while the longitudinal section TEM lamellae were prepared to identify the deformation mechanisms (The workflow for preparing TEM lamella by Fib is displayed in Fig. 3).

3. Results and discussion

To unveil the material removal mechanisms of SLM-ed Ti6Al4V from conventional speed to ultra-high-speed. The surface creation characteristics at various scratching speeds were first investigated. Subsequently, the study focused on the subsurface deformation analysis to reveal the microstructure distribution and evolution under different strain rate conditions. Finally, the chip formation mechanisms regarding chip morphology and microstructure in the chip section were studied to elucidate the removal modes transition with increasing scratching

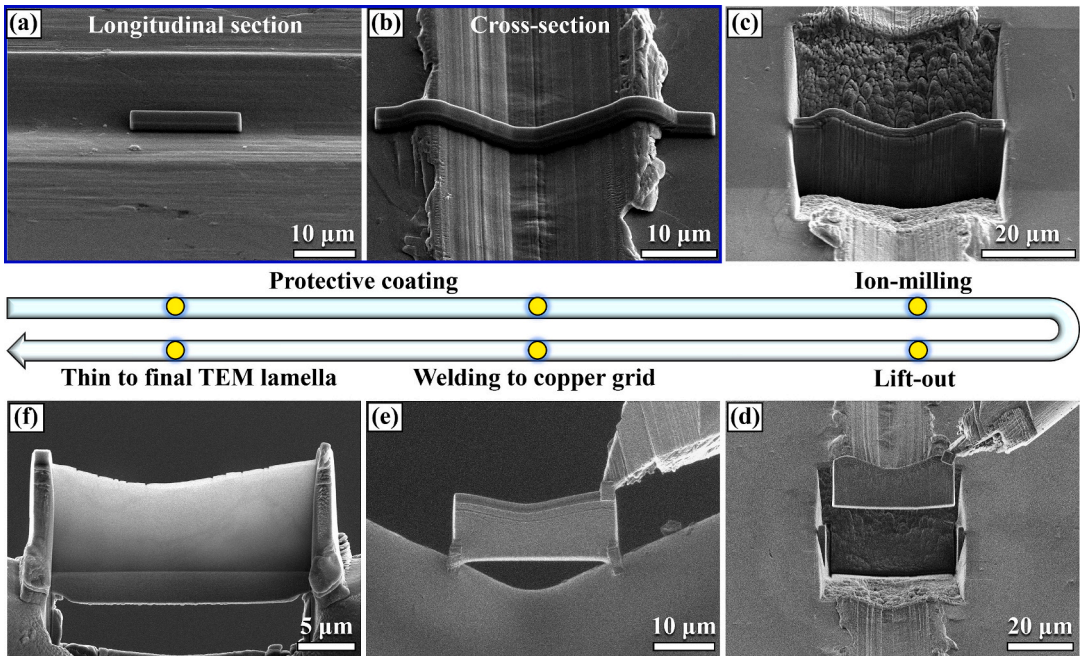

Fig. 3. Workflow for preparing TEM lamella by Fib: (a), (b) Coating carbon layer on the scratch surface to protect the interested surface layer; (c) Ion-milling to expose the interested subsurface area; (d) Lift-out the cross-sectional sample after U cut; (e) Welding the sample to copper grid for further thinning; (f) Repeat thinning with gradually decreasing current.

speed.

3.1. Surface morphology and profile of the scratches made at different speeds

The typical 3D surface morphology and the corresponding average cross-sectional profiles of the scratches made at low to ultra-high speeds are displayed in Fig. 4, d-k. Distinct material pile-ups existed on both sides of single scratches machined at relatively low speeds. These pile-ups were produced due to the plastic deformation of workpiece material under the ploughing effect of the tooltip. However, the material pile-up decreased with the increase in scratching speed. The pile-up ratio R_p is employed to quantitatively evaluate the pile-up effect (The definition of R_p is shown in Fig. 4, a and b). Fig. 4c depicts the statistical results of the pile-up ratio as a function of machining speed. It is revealed that the pile-up ratio linearly decreased from 74.8 % at 20 m/s to 51.6 % at 220 m/s, implying that the cutting effect was strengthened and the material remove rate increased. This is inextricably tied to the material's different responses under varying strain rate conditions [36,37]. The SLM-ed Ti6Al4V exhibited significant plastic deformation under low strain rate loading conditions. However, with an increase in the strain rate, the material flow was significantly suppressed and the material brittleness increased, leading to the suppression of plastic deformation.

3.2. Subsurface microstructure distribution of the scratches made at different machining speeds

Surface finish is a commonly employed criterion for evaluating machining quality. However, a superior surface finish does not necessarily guarantee an improvement in service performance. This is primarily attributed to the substantial influence of subsurface microstructure on mechanical properties [38–40]. In light of this, systematic characterizations combining FIB and STEM were employed to investigate the subsurface microstructure distribution of SLM-ed Ti6Al4V in SPS from conventional speed to ultra-high-speed regions.

The undeformed microstructure of a polished SLM-ed Ti6Al4V sample prior to SPS was first characterized. As illustrated in Fig. 5, the parallel α martensite laths with sparsely distributed dislocations were the dominant microstructure within the prior β grains (Fig. 5, a-c). Furthermore, the compression {10−11} twins were detected between some α laths (Fig. 5, c-f). These internal twins were generated to accommodate the shape strain [41], and this twinning system is commonly observed as the preferred twin structure in Ti6Al4V manufactured by laser AM techniques with high cooling rates and thermal gradients [42]. Additionally, the thickness of the twins varied from a dozen nanometres to more than one hundred nanometres due to the very different local stress conditions.

From the scratch surface made at 20 m/s (Fig. 6a), distinct pile-ups were identified along the scratch edges and small parallel grooves were observed in the scratch surface. To reveal the subsurface plastic deformation induced by scratching, the large cross-sectional TEM samples beneath the scratch were prepared by FIB technique. Based on the global microstructure distribution (Fig. 6b), an MDZ with an average thickness of around 2.8 μm, comprising severely deformed microstructures, was observed. The EDS map of oxygen element (Fig. 6c) indicates oxygen enrichment along the newly formed crack in the interface of the pile-up and the matrix, while the V element shows a uniform distribution (Fig. 6d). To further reveal the microstructure distribution in MDZ, three typical regions, including the scratch's bottom, side wall, and pile-up, were carefully analysed.

In the bottom region of the machined scratch, gradient microstructures were generated under the intense compression impact of the tooltip (Fig. 6e). The topmost layer was full of dynamic recrystallisation (DRX) grains with an average diameter of ~20 nm (Fig. 6f). Beneath the DRX layer, fine elongated grains with multiple substructures such as high-density dislocation tangles or slip bands were identified (Fig. 6g). As for the side wall of the scratch, the microstructure in the topmost layer was also DRX grains. In the deeper layer of MDZ, the grain structures were highly elongated along the direction of the side wall under the extrusion force of the tooltip (Fig. 6, h-j). Furthermore, high material pile-up was produced along the edges of the scratch at conventional machining speed, and cracks were generated as the accumulated material was continuously pushed to the pile-up region (Fig. 6k). The material flow traces can be identified in the pile-up region and its

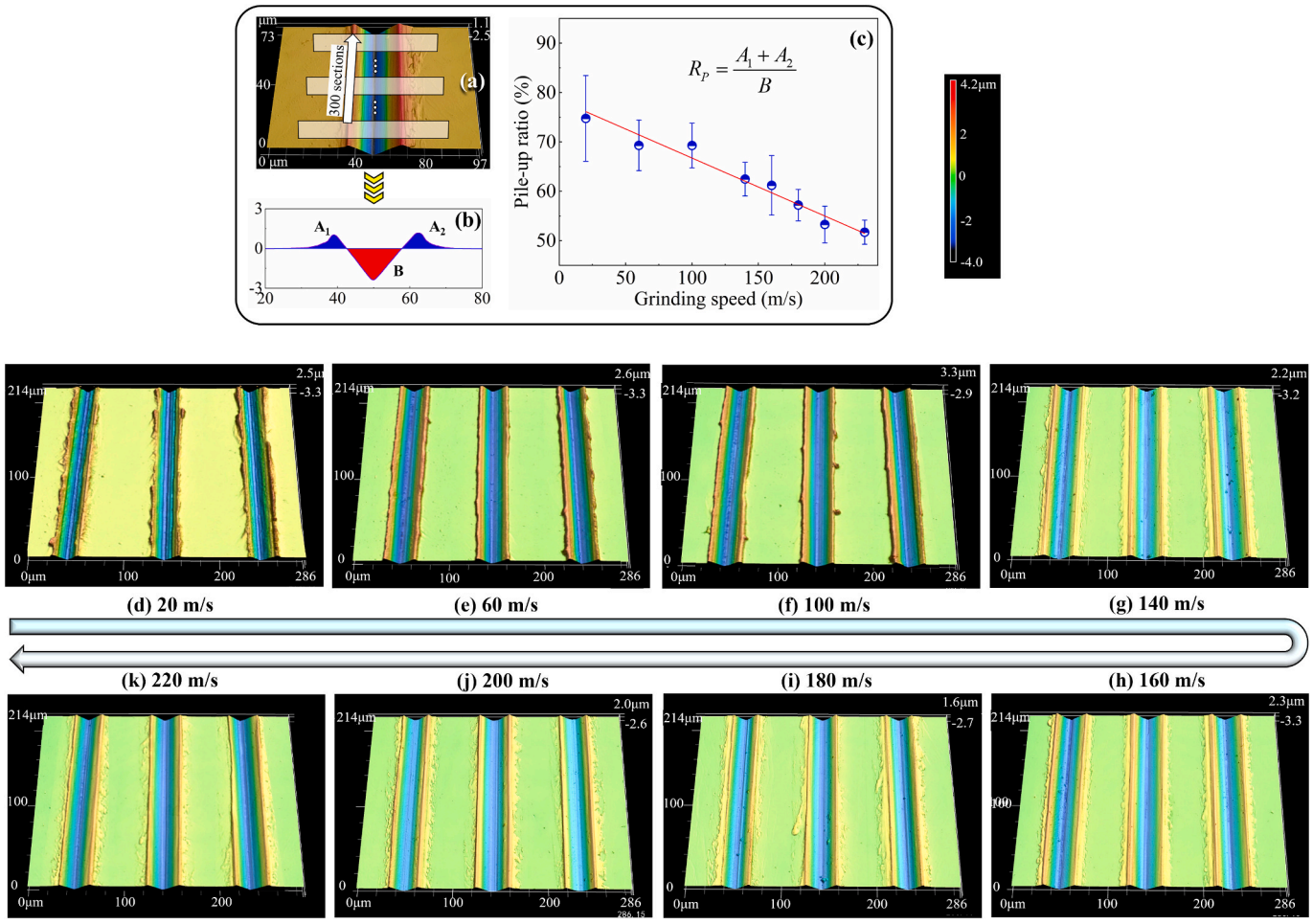

Fig. 4. (a) 300 sections are extracted to generate an average cross-sectional profile; (b) Average cross-sectional profile; (c) Speed effect on the pile-up ratio (R_p is the ratio of the combined area $A_1 + A_2$ to area B); (d-k) 3D surface morphology of scratches machined at different machining speeds and the corresponding cross-sectional profiles.

contiguous areas with the matrix, indicating the occurrence severe plastic deformation (Fig. 6k). Additionally, the grains in the pile-up region were severely deformed, forming bowed nanoscale laths, while the surface layer in contact with the tooltip was full of DRX grains due to the high thermomechanical effect (Fig. 6, l and m).

In contrast to the scratch machined at 20 m/s, the scratch made at 220 m/s exhibited relieved material pile-up and a smooth surface (Fig. 7a). From the subsurface, the MDZ was substantially reduced to ~1 μm (Fig. 7b), which was decreased by 64 % compared to that at 20 m/s. The subsurface displayed a uniform distribution of V element, and no oxygen enrichment occurred in the surface layer (Fig. 7, c and d). Furthermore, different microstructures were observed in the MDZ.

From the bottom of the scratch, it is revealed that the microstructure was severely refined, forming ultrafine grains with a polygonal shape (Fig. 7e). Particularly, high-density lens-like twins were induced within these grains (Fig. 7f). The high-resolution TEM (HRTEM) image in Fig. 7g shows a twin boundary, and the inset FFT pattern identifies that the generated twins as $\{0\bar{1}11\}$ compression twins. In the side wall region of the scratch, a clear boundary between the MDZ and the matrix can be distinguished (Fig. 7h). The enlarged views also reveal the ultrafine grains with embedded twins (UGENTs) structure (Fig. 7, i and j). Additionally, ultrafine grains were generated in the pile-up region, exhibiting an average diameter in the range of 100 to 200 nm (Fig. 7k). Moreover, substructures such as nanoscale twins and dislocations were identified inside the ultrafine grains (Fig. 7l). Similar to the observation at 20 m/s, the high-density dislocations (HDDs) were induced in the α laths in the matrix (Fig. 7m).

Based on the experimental observation of the cross-section of scratches machined at conventional and ultra-high speeds, the plastic deformation layer caused by the thermomechanical impact of the cutting tool notably diminished with an increase in machining speed. The overall MDZ in the subsurface exhibited a “skin effect” as the machining speed increased. Under the conventional speed condition, the material undergoes substantial plastic flow to alleviate the applied energy, with a substantial portion of the plastic deformation energy being transformed into thermal energy [37]. The thermal energy, in turn, subsequently facilitates the plastic deformation by promoting dislocation slip, ultimately resulting in a deep MDZ. However, during the ultra-high-speed deformation, the flow stress of Ti-alloy significantly increases and a higher stress level is required to promote the deformation [25,43]. Meanwhile, the shorter duration of the cutting tool’s action restricts the propagation of stress and heat to the deeper regions due to the faster unloading process. Consequently, the stress/temperature fields tend to be confined within a localization layer [44]. Furthermore, the attenuation of stress waves linearly increases with their frequency [45,46]. Therefore, the high frequency stress wave generated under high strain rate loading experiences rapid attenuation, further confining the stress field to the surface layer. Finally, the MDZ in the ultra-high-speed deformation was significantly reduced. The subsurface damage induced by the machining process adversely affects the performance and reliability of manufactured components, damage controlling is an important research topic in manufacturing processes field [47,48]. The

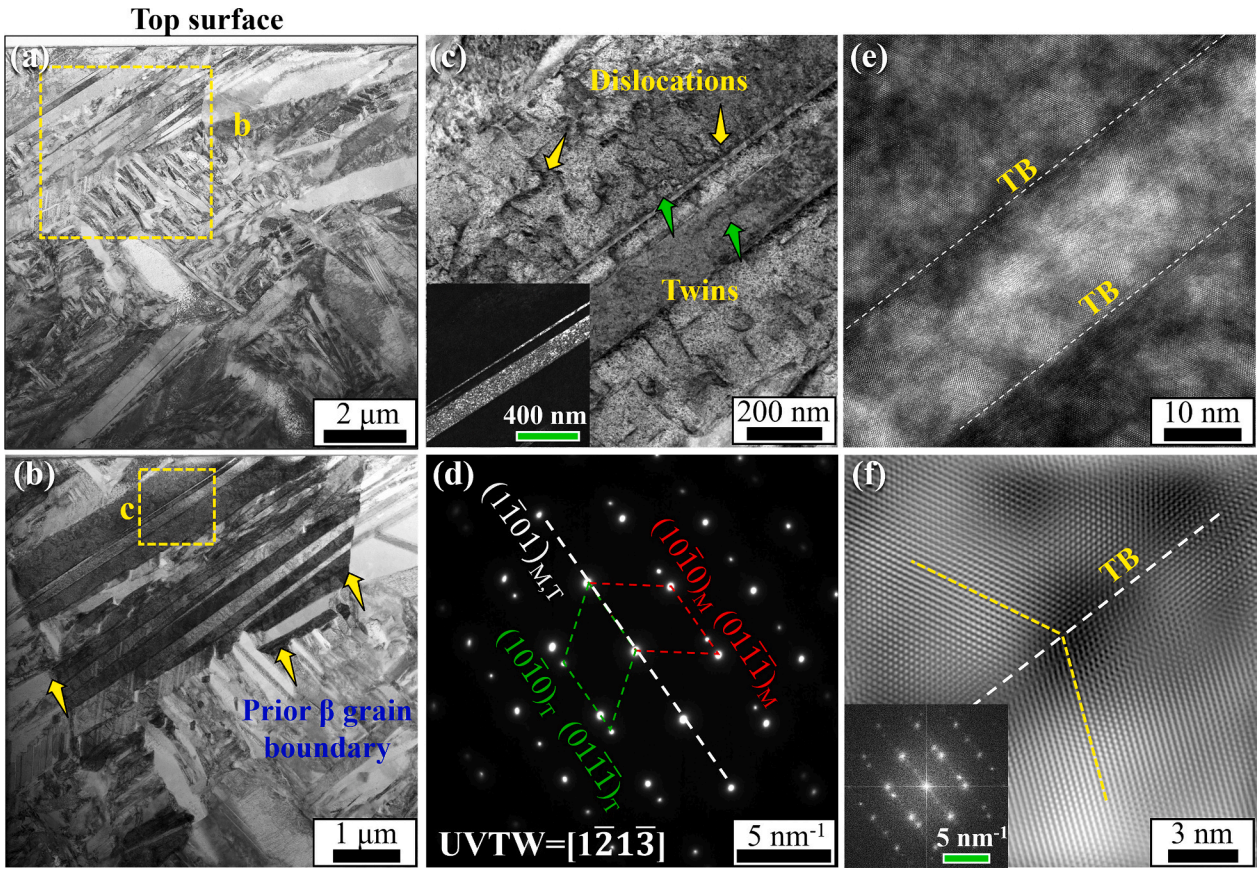

Fig. 5. (a) STEM image of the subsurface microstructure of as-polished Ti6Al4V prior to SPS; (b) Enlarge view depicting the prior β grain boundaries; (c) Twin and dislocation structures (The inset is the corresponding dark-field image); (d) Composite diffraction spots containing the matrix and the twins; (e) HRTEM of the twin; (f) Inverse FFT of the twin interface.

"skin effect" of MDZ under ultra-high speed conditions implies that the subsurface damage induced by the impact of machine tool tends to be confined to the superficial layer, which benefits the control of machining damage in industrial processes.

3.3. Deformation mechanism transition with increasing strain rate

To further investigate the underlying deformation mechanisms and their transitions, this study also characterized the longitudinal TEM samples extracted from the scratches produced at 20, 160, 220 m/s, respectively. Fig. 8 displays the subsurface microstructure in the longitudinal section of scratch machined at 20 m/s. The depth of the MDZ was around 2.6 μm, which is consistent with the observation from the cross-section view. Based on the microstructure features, the MDZ can be divided into two distinct layers. The topmost layer was identified as the DRX zone (DRXZ), distinguished by the presence of equiaxed nanograins (Fig. 8a). The dark-field image in Fig. 8b shows the distribution of the DRX grains. The enlarged view reveals that the DRX grains were surrounded by multiple stacking faults (SFs) (Fig. 8d), suggesting that these grains were formed through the continuous dynamic recrystallisation (CDRX) mechanism [49].

The deeper zone beneath DRXZ was defined as the plastic deformation zone (PDZ), where the microstructure transformed to elongated grains as the reduction of thermomechanical effect (Fig. 8, g and h). Particularly, no distinct boundary existed between the DRXZ and PDZ because the stress and strain rate were progressively changed from the top surface to the subsurface. Instead, a transition microstructure, characterized by the nucleation and formation of ultrafine DRX grains along the boundaries of dislocation cells, was identified in the region between DRXZ and PDZ (Fig. 8, e and f). It can be inferred that these DRX grains were generated following the discontinuous dynamic recrystallisation (DDRX) mechanism [50].

With an increase in scratching speed, the time duration for deformation significantly decreased at higher strain rates, resulting in alterations in the distribution and mechanism of plastic deformation. Fig. 9a shows the plastic deformation distribution of the scratch machined at 160 m/s. The depth of MDZ was decreased to 1.6 μm. Notably, the thickness of PDZ was decreased from 1.7 μm at 20 m/s to 0.9 μm at 160 m/s, indicating a noticeable inhibition effect on plastic deformation. As shown in Fig. 9b, the elongated grains with dislocation tangles (DTs) were observed in the PDZ. Particularly, DRX grains were absent in the topmost layer. Instead, extensive parallel twins were generated in this layer, which is defined as the deformation-induced twin zone (DITZ) (Fig. 9, d-f). The UGENTs structure began to generate in the near surface layer (Fig. 9g), and the HRTEM image further reveals the presence of nano-scale twins within the polygonal UGENTs (Fig. 9h).

As depicted in Fig. 10a, the MDZ in the subsurface of the scratch made at 220 m/s further constrained to a depth of 1 μm from the top surface, and no PDZ existed in the subsurface, indicating a significant inhibition of plastic deformation under the ultra-high strain rate deformation. Furthermore, it is evident that the UGENTs structure was the dominant microstructure in the DITZ. This is consistent with the results observed from the cross-sectional view (Fig. 7). The enlarged view presents a typical UGENTs grain (Fig. 10c). It can be seen that parallel lens-like {0$\bar{1}$11} twins and dislocations were distributed within the ultrafine grain (Fig. 10c-f). Moreover, a typical UGENTs structure with intersected twins was also observed (Fig. 10g, h).

Fig. 11a displays a polygonal nanograin (d < 100 nm) containing inside intersected twins. The STEM morphology and the inset dark-field image show that two sets of parallel nanoscale twins collided, forming V-

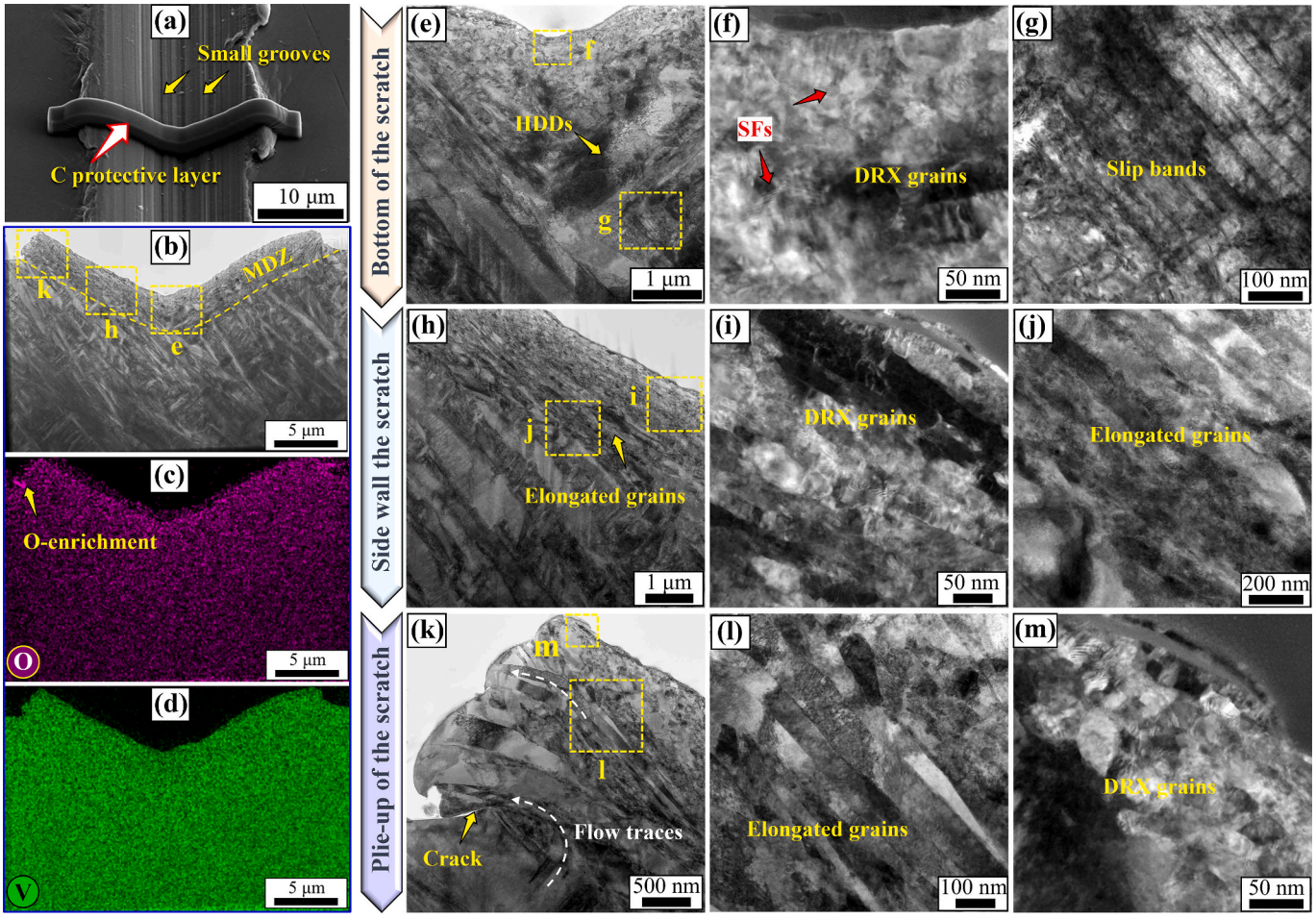

Fig. 6. Cross-section characterization of scratch machined at 20 m/s: (a) Lift out location of cross-sectional sample; (b) STEM image showing the microstructure distribution in the cross-section; (c-d) EDS map of O and V element; (e)-(g) Bottom of the scratch; (h)-(j) Side wall of the scratch; (k)-(m) Plie-up of scratch.

shaped intersected twins. As depicted in the HRTEM image (Fig. 11b), five distinct twins were identified within the nanograin, denoted as T1 to T5. T1, T2, and T3 were paralleled and aligned on the left side, while T4 and T5 aligned on the right side. According to the inverse FFT images and FFT patterns (Fig. 11c-f), the two sets of twins were identified as the $\{0\bar{1}11\}$ twins, and the twin boundaries were the typical coherent twin boundary.

Notably, three-fold twins formed due to the collision of multiple twinning systems. Fig. 11g reveals the intersecting area of T2 and T5. The local boundary between the two intersected twins was also demonstrated as a $\{0\bar{1}11\}$ coherent twin boundary (Fig. 11h), and the two ends of this twin boundaries jointed with TB1, TB3, and TB2, TB4 respectively, forming two three-fold twins. The upper three-fold twin comprised TB1, TB3, and TB5, with an included angle of 120°, while the lower one consisted of TB2, TB4, and TB5, with an included angle of 60°. In contrast to the sequential twinning mechanism of multiple-fold twins under low strain rate conditions [51,52], the extremely high strain rate in this study facilitated the simultaneous activation of multiple twinning systems along $\{0\bar{1}11\}$ planes. Consequently, the collision of two $\{0\bar{1}11\}$ twins led to the formation of three-fold twins.

Plastic deformation is the primary process for metals to alleviate the energy induced by external loads. Two essential mechanisms contribute to this process: dislocation-mediated deformation (DMD) and twin-mediated deformation (TMD) [53]. Generally, dislocation slip is regarded as the prominent deformation mechanism, while twinning serves as the complimentary mechanism [54,55]. However, these two mechanisms compete with each other, and their transition occurs under specific conditions. Numerous studies have demonstrated that the transition from DMD to TMD is significantly influence by various factors. These include the extrinsic factors like deformation temperature, strain rate, as well as the intrinsic factors such as crystal orientation, stacking fault energy (SFE), and grain size [56–58].

According to the STEM characterization of the subsurface microstructure, a transition from dislocation slip to deformation twinning was identified under ultra-high-speed deformation conditions. This phenomenon is intimately connected to the synergistic effect of deformation temperature and strain rate. Generally, lower temperature and/or higher strain rate facilitate the formation of deformation twins [59,60]. During the low-speed machining, the temperature is the dominant factor. The critical stress for dislocation slip (σ_s) is much smaller than that for deformation twining (σ_t). Consequently, the dislocation slip was the dominant deformation mechanism, leading to the formation of DRX and elongated grains at 20 m/s. Notably, no deformation twins were detected (Fig. 8). Furthermore, the σ_s tends to decrease with rising temperature due to the reduction in the shear modulus, while the σ_t remains relatively unchanged despite the variations in temperature [61]. As a result, the increasing machining temperature at higher machining speed makes the dislocation slip the predominant deformation mode across a wide range of machining speeds.

However, with further increase in machining speed, the capacity of dislocations to alleviate deformation becomes inadequate [62]. As dislocation slip involves a continuous and progressive movement of dislocations within a material, the time scale becomes too brief to facilitate dislocation activation at an extremely high strain rate [63]. Meanwhile, high work-hardening and drag force are generated with a

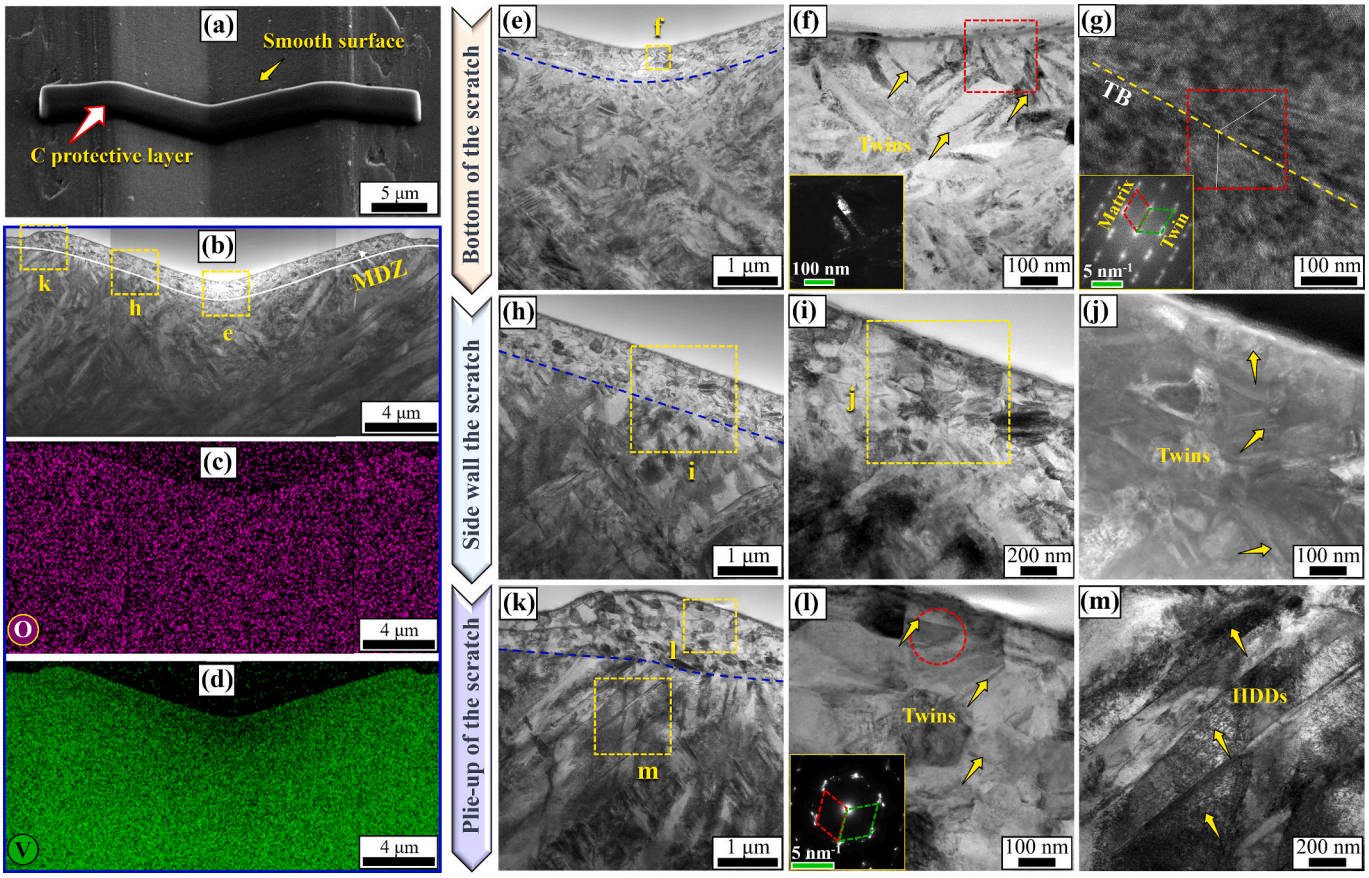

Fig. 7. Cross-section characterization of scratch machined at 220 m/s: (a) Lift out location of cross-sectional sample; (b) STEM image displaying the global cross-section and the corresponding V and O maps; (b)-(d) Bottom of the scratch; (e)-(g) Side wall of the scratch; (h)-(j) Plie-up of scratch.

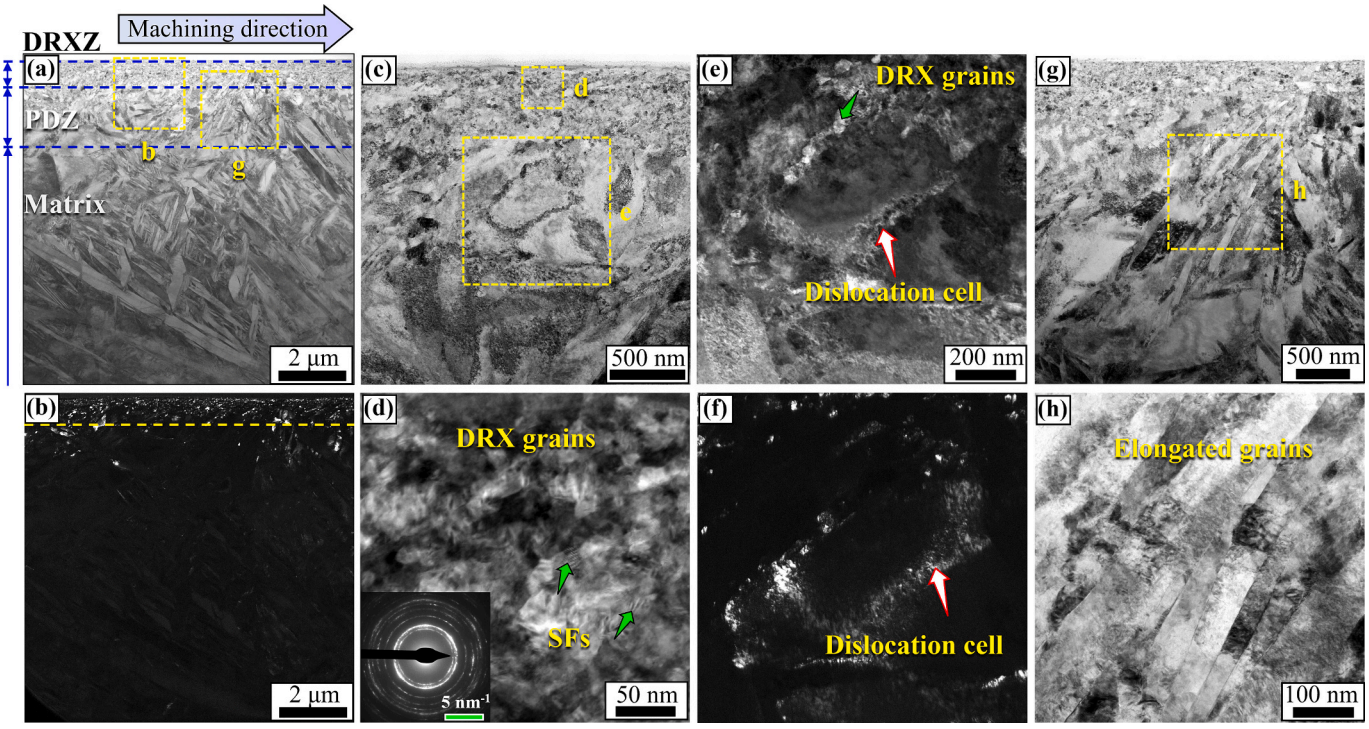

Fig. 8. Subsurface microstructure in longitudinal section of scratch machined at 20 m/s: (a) Plastic deformation distribution; (b) Dark-field image of the DRXZ; (c) MDZ in the near surface; (d) DRX grains in the top surface; (e) Transition microstructure in the region between the DRXZ and PDZ; (f) Dark-field image showing the dislocation cell; (g) Elongated grains in PDZ; (h) Enlarge view of h in (g).

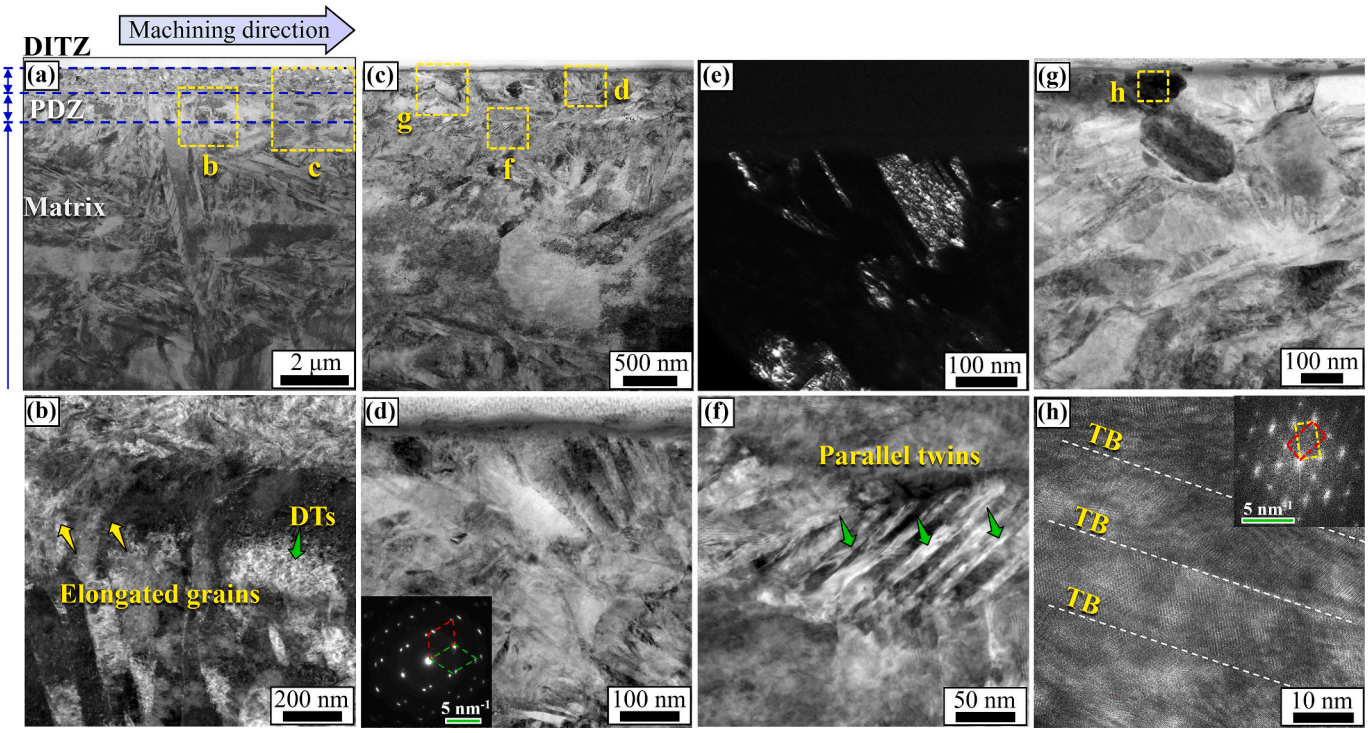

Fig. 9. Subsurface microstructure in longitudinal section of scratch machined at 160 m/s: (a) Plastic deformation distribution; (b) Microstructures in the PDZ; (c) MDZ in the near surface; (d) Nano-twins in the DITZ; (e) Dark-field image of (c); (f) Enlarged view showing parallel twins; (g) UGENTs in topmost layer; (h) HRTEM image displaying the nano-scale twins within the UGENTs.

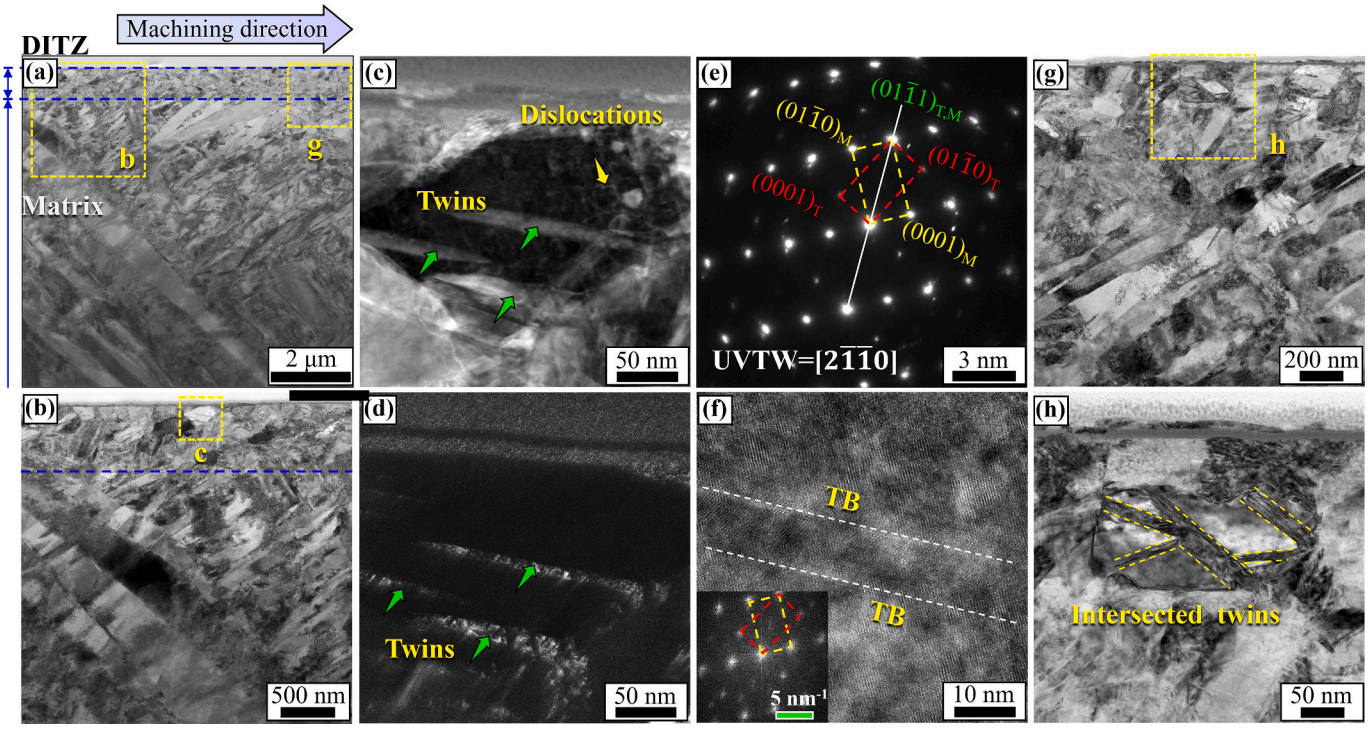

Fig. 10. Subsurface microstructure in longitudinal section of scratch machined at 220 m/s: (a) Plastic deformation distribution; (b) MDZ in the near surface; (c) Nano-twins in an ultrafine grain; (d) Dark-field image of (c); (e) SAED pattern of twins; (f) HRTEM of the twins; (g) Enlarged view of h in (a); (h) Enlarged view showing the intersected twins in an ultrafine grain.

material subjected to high strain rate loading, which impedes the dislocation slip [64]. Conversely, twinning enables abrupt and discrete deformations along twin boundaries, making it a possible deformation-mediated mechanism at ultra-high strain rates. Therefore, deformation twins were induced in the upmost layer of the subsurface of the sample machined at 160 m/s (Fig. 9). Moreover, when the machining speed

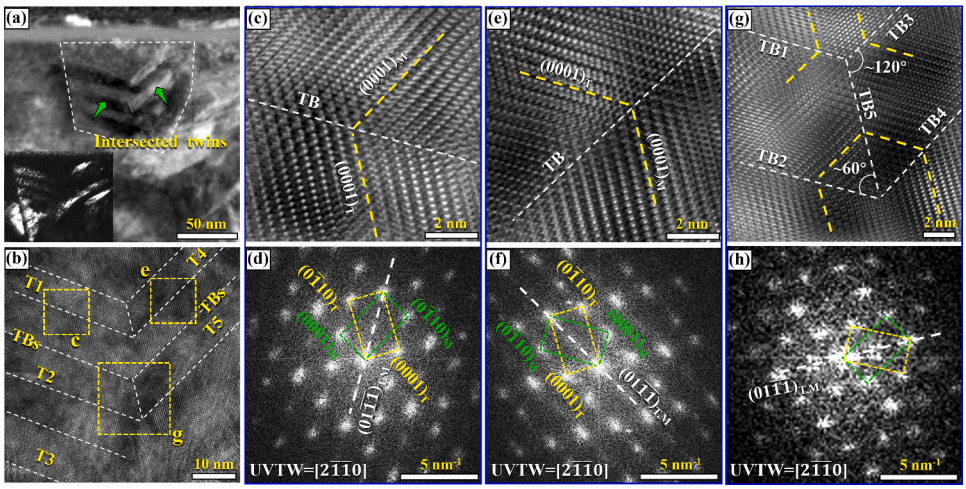

Fig. 11. Twin intersection under ultra-high-speed deformation (220 m/s): (a) Intersected twins in a nanograin (The inset is the dark-field image of twins); (b) HRTEM of the twins (Five twins were labeled as T1 to T5.); (c) Inverse FFT of c in (b); (d) FFT pattern of (c); (e) Inverse FFT of e in (b); (f) FFT pattern of (e); (g) Inverse FFT of g in (b); (h) FFT pattern of (g). (The TBs are indicated by the white-coloured dashed lines, whereas the basal planes are marked by yellow-coloured dashed lines). (For interpretation of the references to colour in this figure legend, the reader is referred to the web version of this article.)

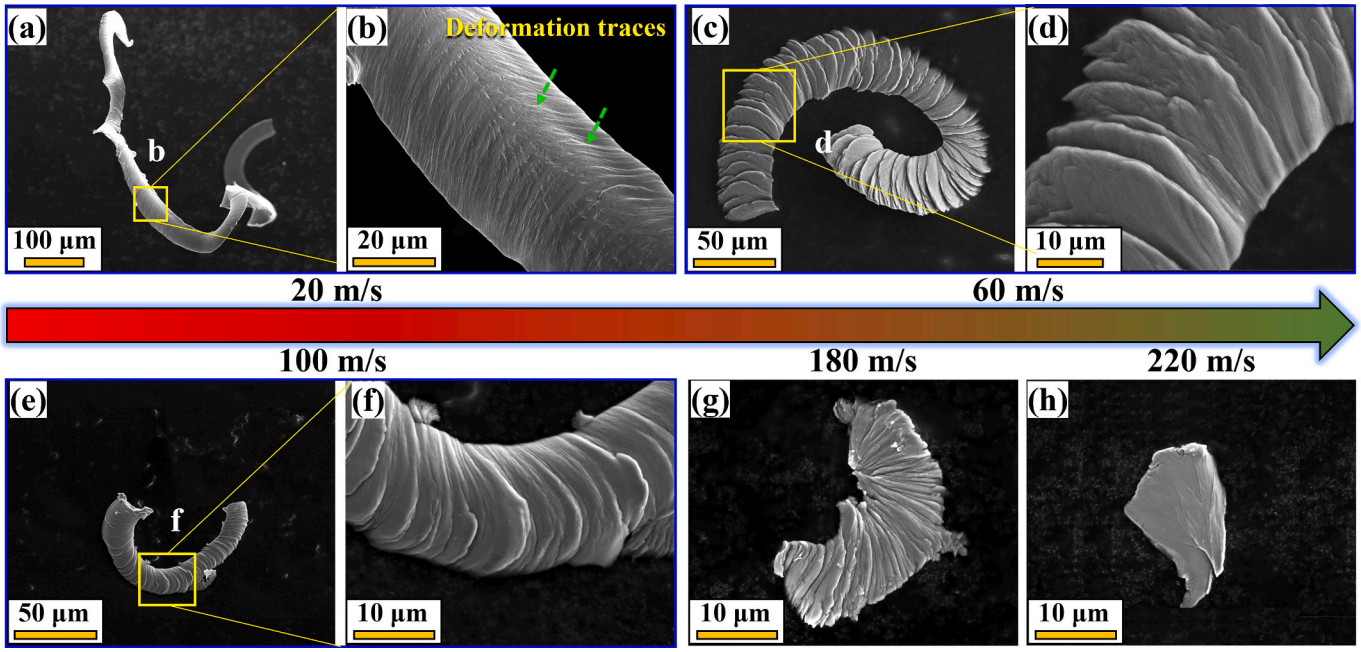

Fig. 12. Chip morphologies of SLM-ed Ti6Al4V at different scratching speeds: (a) Continuous chip at 20 m/s; (b) Enlarged view showing the deformation traces; (c) Segmented chip at 60 m/s; (d) Enlarged view displaying the segments; (e) Segmented chip at 100 m/s; (f) Enlarged view depicting the small segments; (g) Small segmented chip at180 m/s; (g) fragmented chip at 220 m/s.

reached 220 m/s, the PDZ in the subsurface vanished (Fig. 10), and high-density compression {10–11} twins were generated in the deformation layer (Fig. 11), indicating that deformation twinning emerged as the dominant mode of dynamic response under ultra-high strain rate deformation.

In addition, higher temperatures are generally unfavourable for the formation of twins, as the critical shear stress required for twinning (τ_t) tends to increase with temperature in most hcp metals. However, the {10−11} twin is an exceptional type that exhibits a lower critical shear stress (τ_t) at elevated temperatures [65]. This particular characteristic accounts for the presence of {10−11} twins in the matrix of the SLM-ed TiAl4V. Furthermore, it also accelerates the transition from slip-dominated deformation to twinning.

3.4. Chip formation mechanisms at different speeds

Fig. 12 shows the chip morphology of SLM-ed Ti6Al4V produced under varying speed conditions. It is evident that long continuous chips (~1 mm) were generated at 20 m/s, and corrugated deformation traces were observed on the chip free surface (Fig. 12, a and b). As the machining speed increased to 60 m/s, the segmented chips were generated (Fig. 12, c and d), and the chip length decreased to ~300 μm. Furthermore, the shear frequency linearly increases with the increasing in machining speed. Consequently, shorter segmented chips were produced at higher speeds, and their length significantly decreased (Fig. 12, e-g). Notably, the segments tended to separate from each other, forming fragmented chips as the machining speed reached 220 m/s (Fig. 12h).

To reveal the underlying mechanism of chip formation, cross-

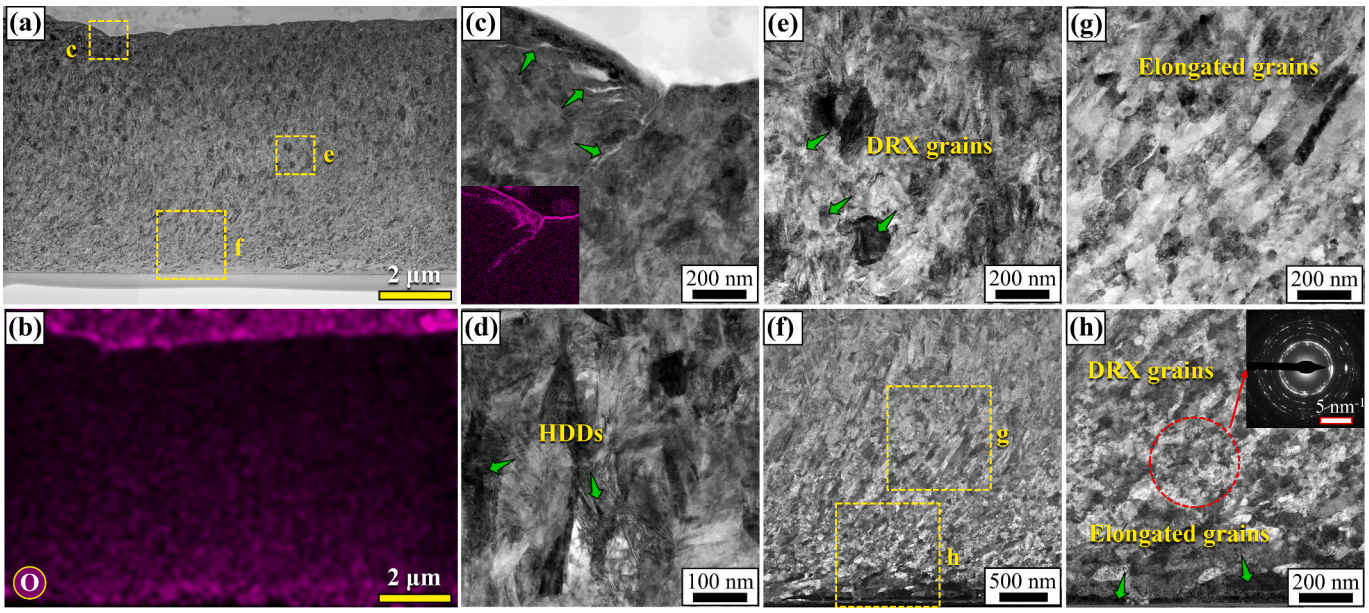

Fig. 13. Section characterization of chip produced at 20 m/s: (a) Microstructure distribution of the global chip section; (b) EDS map of O element; (c) Enlarged view of the free surface area showing the microcracks; (d) HDDs in deformed laminar; (e) Mixed microstructures containing laminar and DRX grains; (f) Microstructures in the area near the chip/tool contact interface; (g) Enlarged view displaying the severely elongated grains; (h) Enlarged view depicting the DRX and elongated grains.

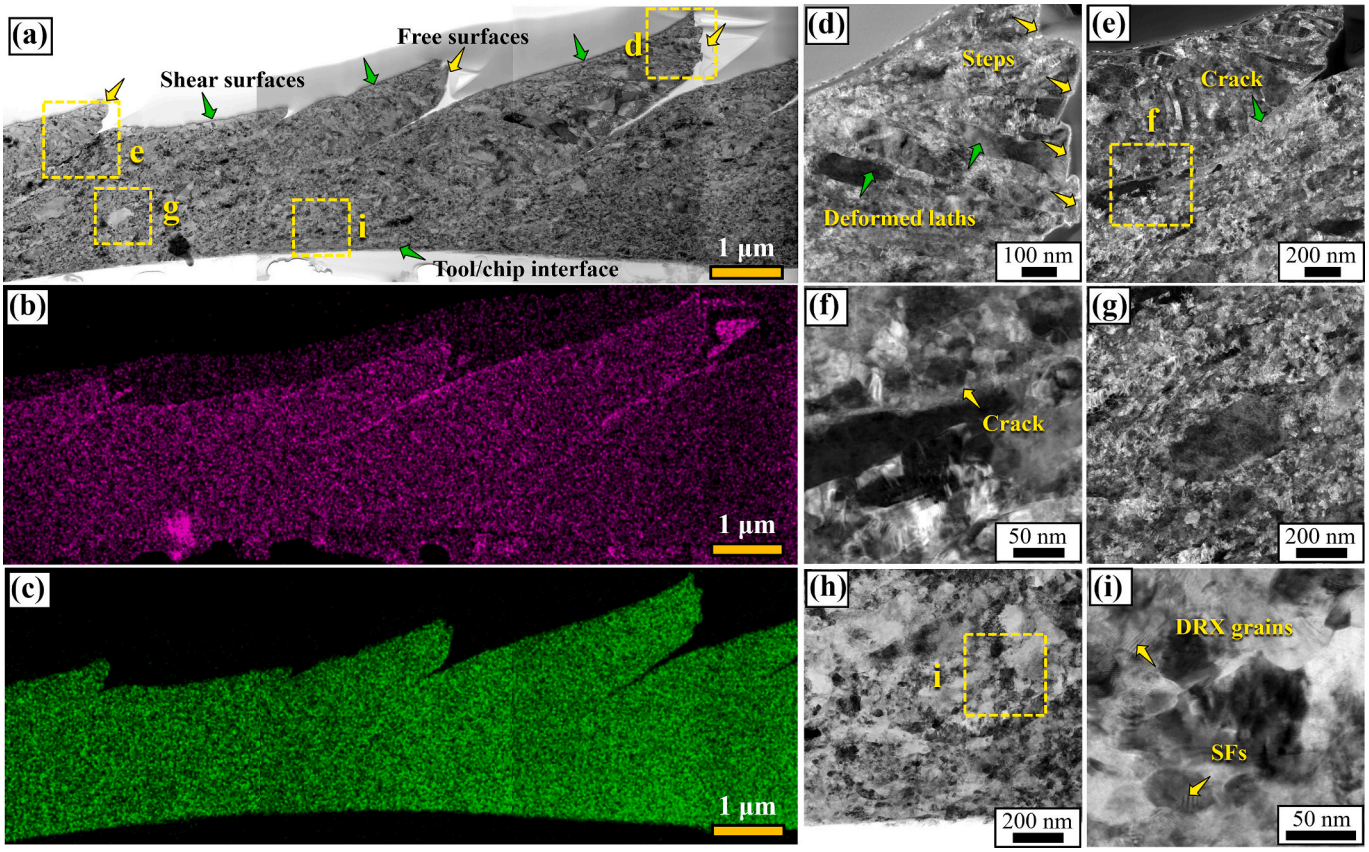

Fig. 14. Section characterization of chip produced at 60 m/s: (a) Microstructure distribution of the global chip section; EDS map of O (b) and V (c) element; (d) Microstructure near the free surface of the segment; (e) Microstructure in the shear region; (f) Ultra-thin shear band; (g) Microstructure in the middle part of the chip section (h) Microstructure in the bottom part of the chip section; (i) Enlarged view showing the DRX grains.

sectional TEM samples of the chips produced at different machining speeds were prepared and characterized. As depicted in Fig. 13a, no distinct segments and adiabatic shear bands (ASBs) were observed in the cross-section of the continuous chip produced at 20 m/s. The EDS map of O element reveals that O enrichment existed along the chip free surface and the chip-tool contact surface (Fig. 13b). The enlarged view indicates

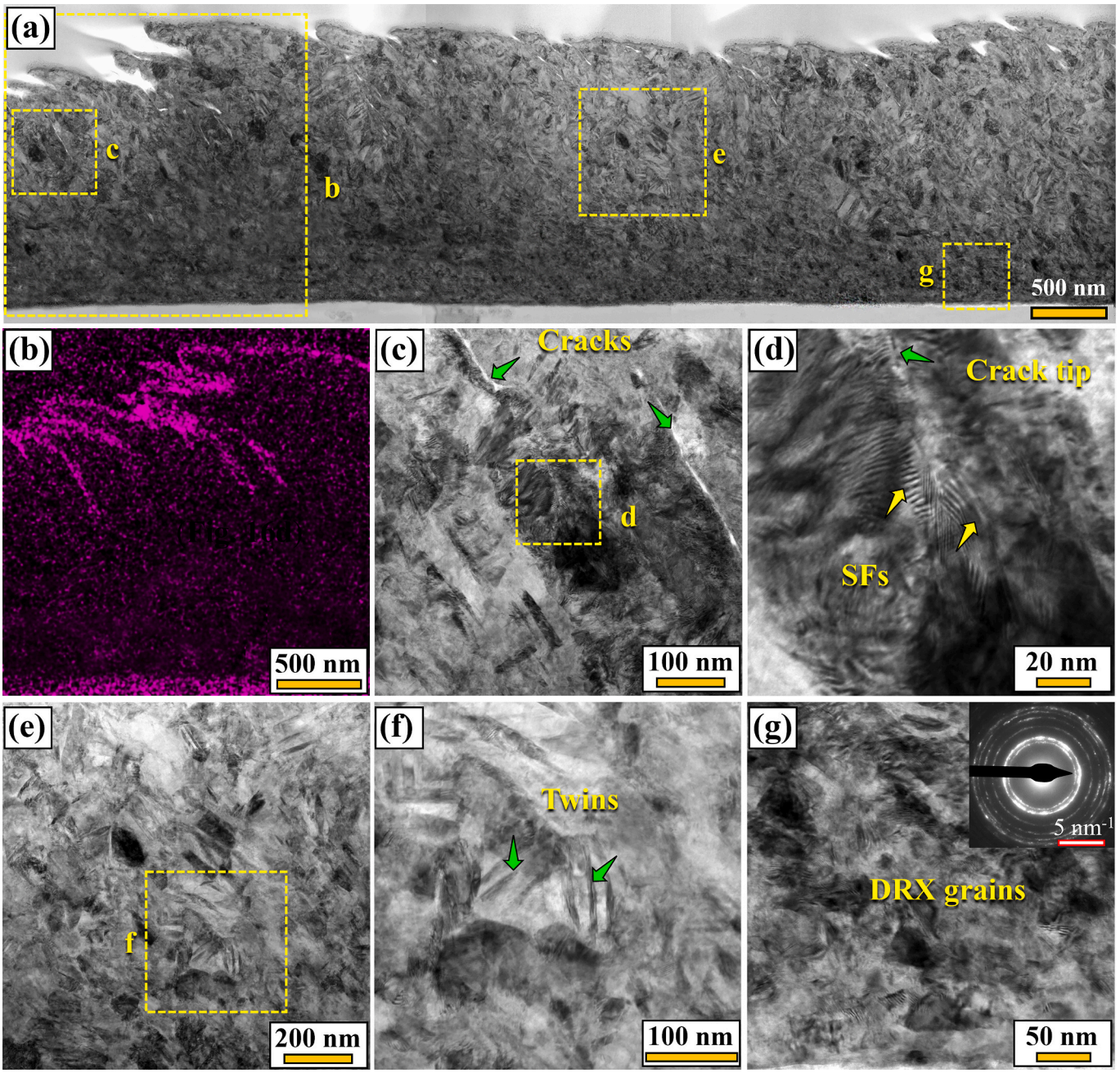

Fig. 15. Section characterization of chip produced at 200 m/s: (a) Microstructure distribution of the global chip section; (b) EDS map of O element of area b in (a); (c) Cracks propagated along the lath boundaries; (d) Microstructure near to the crack tip; (e) Microstructure in the middle part of chip section; (f) Enlarged view showing deformation twins; (g) Microstructure in the bottom part of chip section.

the presence of microcracks beneath the corrugated deformation traces (Fig. 13c). Additionally, the primary microstructure observed in the upper part of the chip section was the deformed laminar structure with HDDs (Fig. 13d). In the middle part of the chip section, a mixed microstructure comprising both deformed laths and DRX grains was produced due to the elevated temperature (Fig. 13e). As plastic deformation intensified in the area closer to the bottom part of the chip section, the mixed microstructure transitioned into highly elongated grains (Fig. 13, f and g). Furthermore, severely refined nanoscale DRX grains with an average diameter of ~30 nm were generated in the lower region, and nanoscale laminar grains were induced in the chip-tool contact surface layer due to severe friction effect (Fig. 13h).

For the segmented chip was generated at 60 m/s, the EDS map of O element (Fig. 14b) reveals that cracks between the adjacent segments were propagated into the middle part of the chip section, indicating the chip was partially segmented. The V element map (Fig. 14c) exhibits a uniform distribution, implying that no distinct phase transformation occurred. In the region near to the free surface, the microstructure primarily comprised deformed laths with inside HDDs. Notably, small steps were observed in the free surface of segments (Fig. 14d), and the edges of the steps were in alignment with the boundaries of laths. It can be inferred that the relative slip along the lath boundaries tended to be activated under the shear loading. These steps facilitated the initiation of cracks under the accumulation of stress and strain, ultimately contributing to the formation of segmented chips.

Fig. 14e presents a typical shear region located between two segments, where a crack initiated from the free surface and propagated into the chip along the shear plane. Notably, an ultra-thin shear band with a

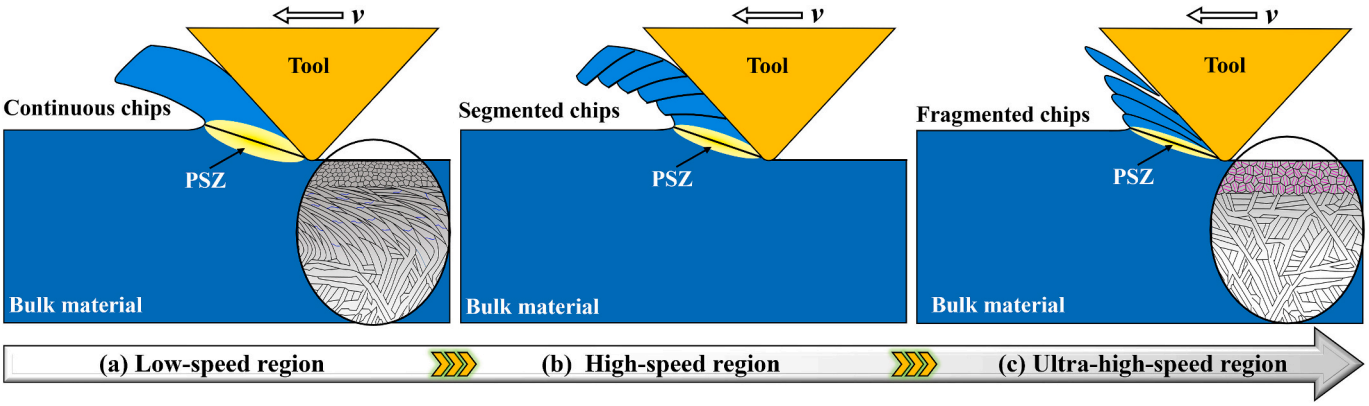

Fig. 16. Schematic of material removal process of SLM-ed Ti6Al4V under different machining speeds: (a) Low speed; (b) High speed; (b) Ultra-high speed.

thickness of approximately 16 nm was observed. The microstructures near to the shear band were ultrafine laths and DRX grains, while no phase transformation was detected in the shear region (Fig. 14f). Additionally, extensive DRX grains were nucleated and formed along the boundaries of elongated grains in the middle part of the chip section (Fig. 14g). And the DRX grains were the dominant microstructure in the region near the tool/chip interface due to the intense thermomechanical effect (Fig. 14, h and i).

Fig. 15a presents the chip section produced at the scratching speed of 200 m/s. Extensive cracks initiated from the free surface in the upper part of the chip section (O map reveals the crack distribution (Fig. 15b)). Furthermore, the cracks were observed propagating along the lath boundaries, and extensive SFs were induced ahead of the crack tip due to the stress concentration (Fig. 15d). Additionally, deformation twins were produced in the chip section due to the very high strain rate (Fig. 15, e and f), and DRX and elongated grains were distributed in the region near the tool/chip contact interface (Fig. 15g).

Based on the experimental results, the material removal processes of SLM-ed Ti6Al4V under different speed conditions are schematically illustrated in Fig. 16. Under low-speed conditions (≤20 m/s), the material underwent relatively uniform deformation in the large primary shear zone (PSZ) under the impact of the tooltip, forming continuous chips without distinct segments (Fig. 16a). Meanwhile, the large deformation affect zone extended to the subsurface, inducing a deep MDZ (Figs. 6 and 8). Generally, Ti6Al4V alloy is highly sensitive to the strain rate of machining, and segmented chips are prone to initiation in wrought Ti6Al4V under low-speed conditions such as several meters per second [66,67]. However, the segmented chips of SLM-ed Ti6Al4V were generated at 60 m/s in this study (Fig. 12). This finding contrasts with the results of previous research, which suggested that SLM-ed Ti6Al4V was more susceptible to adiabatic shearing and exhibited a higher tendency to form segmented chips [68,69]. This discrepancy may be attributed to the transition of material removal mechanisms in wrought and SLM-ed Ti6Al4V.

The formation of segmented chips in wrought Ti6Al4V is primarily due to the activation of ASBs induced by the phase transformation [70]. In contrast, the initiation of segmented chips in SLM-ed Ti6Al4V was driven by the relative slip along the α lath boundaries (Fig. 14). This transition can be attributed to the distinct laminar microstructures in SLM-ed Ti6Al4V, which exhibited higher resistance to deformation at elevated temperatures [71]. As a result, higher stress was required to activate the shear localization behavior. Therefore, SLM-ed Ti6Al4V exhibited a lower tendency to generate segmented chips at low machining speeds. As the machining speed increased to high-speed regions, the shear localization became more pronounced. This was evident from the confinement of the primary shearing zone within a narrower band and a notable increase in segmented frequency. Moreover, the segments tended to separate from each other at ultra-high speeds due to the initiation of extensive cracks, leading to the formation of fragmented chips (Fig. 16c). In this scenario, the material removal process exhibited a brittleness removal mode.

4. Conclusions

This study conducted systematic investigations on the material removal mechanisms of SLM-ed Ti6Al4V over a large speed range, spanning from 20 to 220 m/s. Multiscale characterization methods were combined to detect and analyse the surface creation, subsurface deformation, and chip formation to achieve a comprehensive understanding of the material removal process. The obtained results provide profound insights into the microstructure evolution and deformation mechanisms of SLM-ed Ti6Al4V at different speeds, thus elucidating the transition of material removal mechanisms from low to ultra-high strain rates. The main findings are drawn as follows:

(1) Severe material pile-up was generated during low-speed scratching. However, the pile-up effect was significantly suppressed at higher machining speeds, with the pile-up ratio linearly decreasing from 74.8 % at 20 m/s to 51.6 % at 220 m/s as the machining speed increased;
(2) The depth of the MDZ in SLM-ed Ti6Al4V exhibited a “skin effect” with increasing scratching speed. At a low speed of 20 m/s, a deep MDZ with a depth of 2.8 μm was generated due to severe plastic deformation. In contrast, at 220 m/s, the MDZ was confined to the superficial layer within 1 μm from the top surface due to the significantly suppressed plastic deformation;
(3) Under low strain rate conditions, the microstructure evolution in SLM-ed Ti6Al4V was predominantly governed by dislocation-mediated deformation. The primary microstructures distributed from the top to the subsurface were DRX and elongated grains. However, with the increase in strain rate, a transition of deformation mechanism from dislocation slip to twinning was identified. Twinning-mediated deformation emerged as the dominant mode under the ultra-high strain rate deformation, leading to the formation of a novel UGENTs microstructure;
(4) SLM-ed Ti6Al4V displayed different material removal modes from low to ultra-high-speed regions. At low scratching speeds (≤20 m/s), the material was removed in the form of continuous chips. As the scratching speed increased to 60 m/s, segmented chips were generated driven by relative slip along the α lath boundaries. Notably, fragmented chips tended to form as the segmented chips separated at the highest scratching speed of 220 m/s.

CRediT authorship contribution statement

Qinghong Jiang: Writing – review & editing, Writing – original draft, Visualization, Validation, Software, Methodology, Investigation, Formal analysis, Data curation, Conceptualization. **Shuai Li:** Writing – review & editing, Software. **Hao Liu:** Writing – review & editing, Software. **Mingwang Fu:** Writing – review & editing, Supervision, Project administration, Funding acquisition. **Bi Zhang:** Writing – review & editing, Supervision, Project administration, Funding acquisition, Conceptualization.

Declaration of competing interest

The authors declare that they have no known competing financial interests or personal relationships that could have appeared to influence the work reported in this paper.

Acknowledgement

The authors acknowledge the assistance from SUSTech Core Research Facilities. This work was supported by Shenzhen Science and Technology Innovation Commission for the project numbered KQTD20190929172505711, Guangdong Provincial Department of Science and Technology grant 2019JC01Z031, Guangdong Collaborative Fund for Basic and Applied Research 2021B1515120009, and the project from the Hong Kong Polytechnic University Grant 1-ZE1W, National Natural Science Foundation of China grant 51835011, General Research Fund 15229922.

References

[1] Zhao Q, Sun Q, Xin S, Chen Y, Wu C, Wang H, et al. High-strength titanium alloys for aerospace engineering applications: a review on melting-forging process. Mater Sci Eng A 2022;845:143260. https://doi.org/10.1016/j.msea.2022.143260.
[2] Guerra-Yánez H, Florido-Suárez NR, Voiculescu I, Mirza-Rosca JC. Corrosion behavior of new titanium alloys for medical applications. Mater Today Proc 2023; 72:533–7. https://doi.org/10.1016/j.matpr.2022.08.112.
[3] Wu Z, Kou H, Chen N, Xi Z, Fan J, Tang B, et al. Recent developments in cold dwell fatigue of titanium alloys for aero-engine applications: a review. J Mater Res Technol 2022;20:469–84. https://doi.org/10.1016/j.jmrt.2022.07.094.
[4] Pereira T, Kennedy JV, Potgieter J. A comparison of traditional manufacturing vs additive manufacturing, the best method for the job. Procedia Manuf 2019;30: 11–8. https://doi.org/10.1016/j.promfg.2019.02.003.
[5] Lu J, Zhuo L. Additive manufacturing of titanium alloys via selective laser melting: fabrication, microstructure, post-processing, performance and prospect. International Int J Refract Met Hard Mater International 2023;111:106110. https://doi.org/10.1016/j.ijrmhm.2023.106110.
[6] Aufa AN, Hassan MZ, Ismail Z. Recent advances in Ti-6Al-4V additively manufactured by selective laser melting for biomedical implants: prospect development. J Alloys Compd 2022;896:163072. https://doi.org/10.1016/j.jallcom.2021.163072.
[7] Armstrong M, Mehrabi H, Naveed N. An overview of modern metal additive manufacturing technology. J Manuf Process 2022;84:1001–29. https://doi.org/10.1016/j.jmapro.2022.10.060.
[8] Batalha GF, Silva LC, Coelho RS, Teixeira MCC, Castro TL, Pereira MVS, et al. Mechanical properties characterization of Ti-6Al-4 V grade 5 (recycled) additively manufactured by selective electron beam melting (EB-PBF). Eng Fail Anal 2024; 157:107892. https://doi.org/10.1016/j.engfailanal.2023.107892.
[9] Kokare S, Oliveira JP, Godina R. A LCA and LCC analysis of pure subtractive manufacturing, wire arc additive manufacturing, and selective laser melting approaches. J Manuf Process 2023;101:67–85. https://doi.org/10.1016/j.jmapro.2023.05.102.
[10] Pratheesh Kumar S, Elangovan S, Mohanraj R, Ramakrishna JR. Review on the evolution and technology of State-of-the-Art metal additive manufacturing processes. Mater Today Proc 2021;46:7907–20. https://doi.org/10.1016/j.matpr.2021.02.567.
[11] Pal S, Lojen G, Hudak R, Rajtukova V, Brajlih T, Kokol V, et al. As-fabricated surface morphologies of Ti-6Al-4V samples fabricated by different laser processing parameters in selective laser melting. Addit Manuf 2020;33:101147. https://doi.org/10.1016/j.addma.2020.101147.
[12] Zhang B, Li Y, Bai Q. Defect formation mechanisms in selective laser melting: a review. Chin J Mech Eng 2017;30:515–27. https://doi.org/10.1007/s10033-017-0121-5.
[13] Khairallah SA, Martin AA, Lee JR, Guss G, Calta NP, Hammons JA, et al. Controlling interdependent meso-nanosecond dynamics and defect generation in metal 3D printing. Science 2020;368:660–5. https://doi.org/10.1126/science.aay7830.
[14] Malakizadi A, Mallipeddi D, Dadbakhsh S, M'Saoubi R, Krajnik P. Post-processing of additively manufactured metallic alloys – a review. Int J Mach Tools Manuf 2022;179:103908. https://doi.org/10.1016/j.ijmachtools.2022.103908.
[15] Jamil M, He N, Gupta MK, Zhao W, Khan AM. Tool wear mechanisms and its influence on machining tribology of face milled titanium alloy under sustainable hybrid lubri-cooling. Tribol Int 2022;170:107497. https://doi.org/10.1016/j.triboint.2022.107497.
[16] Liang X, Liu Z, Wang B. State-of-the-art of surface integrity induced by tool wear effects in machining process of titanium and nickel alloys: a review. Measurement 2019;132:150–81. https://doi.org/10.1016/j.measurement.2018.09.045.
[17] Al-Rubaie KS, Melotti S, Rabelo A, Paiva JM, Elbestawi MA, Veldhuis SC. Machinability of SLM-produced Ti6Al4V titanium alloy parts. J Manuf Process 2020;57:768–86. https://doi.org/10.1016/j.jmapro.2020.07.035.
[18] Polishetty A, Shunmugavel M, Goldberg M, Littlefair G, Singh RK. Cutting force and surface finish analysis of machining additive manufactured titanium alloy Ti-6Al-4V. Procedia Manuf 2017;7:284–9. https://doi.org/10.1016/j.promfg.2016.12.071.
[19] Li G, Chandra S, Rahman Rashid RA, Palanisamy S, Ding S. Machinability of additively manufactured titanium alloys: a comprehensive review. J Manuf Process 2022;75:72–99. https://doi.org/10.1016/j.jmapro.2022.01.007.
[20] Zhang B, Yin J. The 'skin effect'of subsurface damage distribution in materials subjected to high-speed machining. Int J Extreme Manuf 2019;1:012007. https://doi.org/10.1088/2631-7990/ab103b.
[21] Yang X, Zhang B. Material embrittlement in high strain-rate loading. Int J Extreme Manuf 2019;1:022003. https://doi.org/10.1088/2631-7990/ab263f.
[22] Wang B, Liu Z, Su G, Ai X. Brittle removal mechanism of ductile materials with ultrahigh-speed machining. J Manuf Sci Eng 2015;137:061002. https://doi.org/10.1115/1.4030826.
[23] Guo S, Zhang J, Jiang Q, Zhang B. Surface integrity in high-speed grinding of Al6061T6 alloy. CIRP Ann 2022;71:281–4. https://doi.org/10.1016/j.cirp.2022.03.002.
[24] Guo S, Lu S, Zhang B, Cheung CF. Surface integrity and material removal mechanisms in high-speed grinding of Al/SiCp metal matrix composites. Int J Mach Tools Manuf 2022;178:103906. https://doi.org/10.1016/j.ijmachtools.2022.103906.
[25] Hu H, Xu Z, Dou W, Huang F. Effects of strain rate and stress state on mechanical properties of Ti-6Al-4V alloy. Int J Impact Eng 2020;145:103689. https://doi.org/10.1016/j.ijimpeng.2020.103689.
[26] Chen L, Pan L, Xuan H, Sun Z, Niu X, Song Y, et al. High strain rate mechanical behavior of Ti-6Al-4V with micro–macro correlation under compressive loading. Eng Fail Anal 2024;157:107913. https://doi.org/10.1016/j.engfailanal.2023.107913.
[27] Salvado FC, Teixeira-Dias F, Walley SM, Lea LJ, Cardoso JB. A review on the strain rate dependency of the dynamic viscoplastic response of FCC metals. Prog Mater Sci 2017;88:186–231. https://doi.org/10.1016/j.pmatsci.2017.04.004.
[28] Wang B, Liu Z, Cai Y, Luo X, Ma H, Song Q, et al. Advancements in material removal mechanism and surface integrity of high speed metal cutting: a review. Int J Mach Tools Manuf 2021;166:103744. https://doi.org/10.1016/j.ijmachtools.2021.103744.
[29] Sutter G, List G. Very high speed cutting of Ti-6Al-4V titanium alloy - change in morphology and mechanism of chip formation. Int J Mach Tools Manuf 2013;66: 37–43. https://doi.org/10.1016/j.ijmachtools.2012.11.004.
[30] Wang Q, Liu Z. Plastic deformation induced nano-scale twins in Ti-6Al-4V machined surface with high speed machining. Mater Sci Eng A 2016;675:271–9. https://doi.org/10.1016/j.msea.2016.08.076.
[31] Fang W, Wang J, Cai F, Chen J, Gyawali G, Zhang S. Effects of multilayer structure on impacting fatigue resistance and high-speed dry cutting performance against Ti-6Al-4 V of AlTiN/AlTiBN multilayer coatings. Tribol Int 2024;192:109258. https://doi.org/10.1016/j.triboint.2024.109258.
[32] Zhang L, Zhang X. A comparative experimental study of unidirectional CFRP high-speed milling in up and down milling with varied angles. J Manuf Process 2023; 101:1147–57. https://doi.org/10.1016/j.jmapro.2023.06.064.
[33] Öpöz TT, Chen X. Experimental investigation of material removal mechanism in single grit grinding. Int J Mach Tools Manuf 2012;63:32–40. https://doi.org/10.1016/j.ijmachtools.2012.07.010.
[34] Zhao B, Jiang G, Ding W, Xiao G, Huan H, Wang Y, et al. Characterisation of the wear properties of a single-aggregated cubic boron nitride grain during Ti–6Al–4V alloy grinding. Wear 2020;452-453:203296. https://doi.org/10.1016/j.wear.2020.203296.
[35] Jiang Q, Li S, Guo S, Fu M, Zhang B. Comparative study on process-structure-property relationships of TiC/Ti6Al4V and Ti6Al4V by selective laser melting. Int J Mech Sci 2023;241:107963. https://doi.org/10.1016/j.ijmecsci.2022.107963.
[36] Wang B, Liu Z, Su G, Song Q, Ai X. Investigations of critical cutting speed and ductile-to-brittle transition mechanism for workpiece material in ultra-high speed machining. Int J Mech Sci 2015;104:44–59. https://doi.org/10.1016/j.ijmecsci.2015.10.004.
[37] Zhou L, Shimizu J, Muroya A, Eda H. Material removal mechanism beyond plastic wave propagation rate. Precis Eng 2003;27:109–16. https://doi.org/10.1016/S0141-6359(02)00124-1.
[38] la Monaca A, Murray JW, Liao Z, Speidel A, Robles-Linares JA, Axinte DA, et al. Surface integrity in metal machining - part II: functional performance. Int J Mach Tools Manuf 2021;164:103718. https://doi.org/10.1016/j.ijmachtools.2021.103718.
[39] Javidi A, Rieger U, Eichlseder W. The effect of machining on the surface integrity and fatigue life. Int J Fatigue 2008;30:2050–5. https://doi.org/10.1016/j.ijfatigue.2008.01.005.

[40] Liao Z, la Monaca A, Murray J, Speidel A, Ushmaev D, Clare A, et al. Surface integrity in metal machining - part I: fundamentals of surface characteristics and formation mechanisms. Int J Mach Tools Manuf 2021;162:103687. https://doi.org/10.1016/j.ijmachtools.2020.103687.
[41] Zhong HZ, Zhang XY, Wang SX, Gu JF. Examination of the twinning activity in additively manufactured Ti-6Al-4V. Mater Des 2018;144:14–24. https://doi.org/10.1016/j.matdes.2018.02.015.
[42] Pantawane MV, Sharma S, Sharma A, Dasari S, Banerjee S, Banerjee R, et al. Coarsening of martensite with multiple generations of twins in laser additively manufactured Ti6Al4V. Acta Mater 2021;213:116954. https://doi.org/10.1016/j.actamat.2021.116954.
[43] George TGI. High-strain-rate deformation: mechanical behavior and deformation substructures induced. Annu Rev Mater Res 2012;42:285–303. https://doi.org/10.1146/annurev-matsci-070511-155034.
[44] Yan N, Li Z, Xu Y, Meyers MA. Shear localization in metallic materials at high strain rates. Prog Mater Sci 2021;119:100755. https://doi.org/10.1016/j.pmatsci.2020.100755.
[45] Oda H, Nishizawa O, Kusunose KI, Hirata T. Frequency-dependence of velocity and attenuation of elastic waves in granite under uniaxial compression. Pure Appl Geophys 1990;133:73–85. https://doi.org/10.1007/BF00876703.
[46] Liu C, Ahrens T. Stress wave attenuation in shock-damaged rock. J Geophys Res Solid Earth 1997;102:5243–50. https://doi.org/10.1029/96JB03891.
[47] Zhou Y, Wang S, Chen H, Zou J, Ma L, Yin G. Study on surface quality and subsurface damage mechanism of nickel-based single-crystal superalloy in precision turning. J Manuf Process 2023;99:230–42. https://doi.org/10.1016/j.jmapro.2023.05.053.
[48] Yan A, Zhang H, Deng B, Peng F, Yan R, Cui F. Analytical modeling of subsurface damage in laser-assisted machining of metal matrix composites based on the reinforcement fracture probability. J Manuf Process 2024;109:300–12. https://doi.org/10.1016/j.jmapro.2023.12.001.
[49] Huang K, Logé RE. A review of dynamic recrystallization phenomena in metallic materials. Mater Des 2016;111:548–74. https://doi.org/10.1016/j.matdes.2016.09.012.
[50] Zhong X, Huang L, Liu F. Discontinuous dynamic recrystallization mechanism and twinning evolution during hot deformation of Incoloy 825. J Mater Eng Perform 2020;29:6155–69. https://doi.org/10.1007/s11665-020-05093-1.
[51] Zhu Q, Huang Q, Tian Y, Zhao S, Chen Y, Cao G, et al. Hierarchical twinning governed by defective twin boundary in metallic materials. Sci Adv 2022;8:eabn8299. https://doi.org/10.1126/sciadv.abn8299.
[52] Zhang Z, Huang S, Chen L, Zhu Z, Guo D. Formation mechanism of fivefold deformation twins in a face-centered cubic alloy. Sci Rep 2017;7:45405. https://doi.org/10.1038/srep45405.
[53] Qi YW, Luo ZP, Li XY, Lu K. Transition of deformation mechanisms from twinning to dislocation slip in nanograined pure cobalt. J Mater Sci Technol 2022;121:124–9. https://doi.org/10.1016/j.jmst.2022.02.009.
[54] Vinogradov A, Vasilev E, Linderov M, Merson D. In situ observations of the kinetics of twinning–detwinning and dislocation slip in magnesium. Mater Sci Eng A 2016;676:351–60. https://doi.org/10.1016/j.msea.2016.09.004.
[55] Sun C, Guo N, Fu M, Wang S. Modeling of slip, twinning and transformation induced plastic deformation for TWIP steel based on crystal plasticity. Int J Plast 2016;76:186–212. https://doi.org/10.1016/j.ijplas.2015.08.003.
[56] Cai T, Zhang Z, Zhang P, Yang JB, Zhang Z. Competition between slip and twinning in face-centered cubic metals. J Appl Phys 2014;116:163512. https://doi.org/10.1063/1.4898319.
[57] Zhu YT, Liao XZ, Wu XL, Narayan J. Grain size effect on deformation twinning and detwinning. J Mater Sci 2013;48:4467–75. https://doi.org/10.1007/s10853-013-7140-0.
[58] Meyers MA, Vöhringer O, Lubarda VA. The onset of twinning in metals: a constitutive description. Acta Mater 2001;49:4025–39. https://doi.org/10.1016/S1359-6454(01)00300-7.
[59] Zhao S, Zhang R, Yu Q, Ell J, Ritchie RO, Minor AM. Cryoforged nanotwinned titanium with ultrahigh strength and ductility. Science 2021;373:1363–8. https://doi.org/10.1126/science.abe7252.
[60] Dai L, Song W. A strain rate and temperature-dependent crystal plasticity model for hexagonal close-packed (HCP) materials: application to α-titanium. Int J Plast 2022;154:103281. https://doi.org/10.1016/j.ijplas.2022.103281.
[61] Maria dV Nicolò, Peter S, Amit S, Manish J, Cinzia P. Micromechanical response of pure magnesium at different strain rate and temperature conditions: twin to slip and slip to twin transitions. Acta Mater 2023;243:118528. https://doi.org/10.1016/j.actamat.2022.118528.
[62] Zepeda-Ruiz LA, Stukowski A, Oppelstrup T, Bulatov VV. Probing the limits of metal plasticity with molecular dynamics simulations. Nature 2017;550:492–5. https://doi.org/10.1038/nature23472.
[63] Gurrutxaga-Lerma B, Balint DS, Dini D, Sutton AP. The mechanisms governing the activation of dislocation sources in aluminum at different strain rates. J Mech Phys Solids 2015;84:273–92. https://doi.org/10.1016/j.jmps.2015.08.008.
[64] Yan Z, Wang L, Ning Z, Li Y, Liu A, Cheng X. Evolution of dislocations and deformation twins in Ti6321 titanium alloy under contact explosion. J Mater Res Technol 2023;24:1070–5. https://doi.org/10.1016/j.jmrt.2023.03.027.
[65] Paton NE, Backofen WA. Plastic deformation of titanium at elevated temperatures. Int J Plast 1970;1:2839–47. https://doi.org/10.1007/BF03037822.
[66] Ye GG, Xue SF, Jiang MQ, Tong XH, Dai LH. Modeling periodic adiabatic shear band evolution during high speed machining Ti-6Al-4V alloy. Int J Plast 2013;40:39–55. https://doi.org/10.1016/j.ijplas.2012.07.001.
[67] Palaniappan K, Sundararaman M, Murthy H, Jeyaraam R, Rao BC. Influence of workpiece texture and strain hardening on chip formation during machining of Ti–6Al–4V alloy. Int J Mach Tools Manuf 2022;173:103849. https://doi.org/10.1016/j.ijmachtools.2021.103849.
[68] Shunmugavel M, Goldberg M, Polishetty A, Nomani J, Sun S, Littlefair G. Chip formation characteristics of selective laser melted Ti–6Al–4V. Aust J Mech Eng 2019;17:109–26. https://doi.org/10.1080/14484846.2017.1364833.
[69] Kishawy HA, Nguyen N, Hosseini A, Elbestawi M. Machining characteristics of additively manufactured titanium, cutting mechanics and chip morphology. CIRP Ann 2023;72:49–52. https://doi.org/10.1016/j.cirp.2023.04.056.
[70] Zhang XP, Shivpuri R, Srivastava AK. Role of phase transformation in chip segmentation during high speed machining of dual phase titanium alloys. J Mater Process Technol 2014;214:3048–66. https://doi.org/10.1016/j.jmatprotec.2014.07.007.
[71] Motoyama Y, Tokunaga H, Kajino S, Okane T. Stress–strain behavior of a selective laser melted Ti-6Al-4V at strain rates of 0.001–1/s and temperatures 20–1000 °C. J Mater Process Technol 2021;294:117141. https://doi.org/10.1016/j.jmatprotec.2021.117141.